Expert Systems With Applications 290 (2025) 128352

Contents lists available at ScienceDirect

Expert Systems With Applications

journal homepage: www.elsevier.com/locate/eswa

Advanced optimization of thermal efficiency in low-low temperature economizers and air heater system employing the crested porcupine optimizer algorithm

Huaan Li [a], Dongliang Wei [a], Yajie Wu [a], Hui Li [b], Hongtao Liu [b], Xiaolin Hu [b], Huanxiang Zhang [b], Hao Zhou [a,*]

[a] Zhejiang University, Institute for Thermal Power Engineering, State Key Laboratory of Clean Energy Utilization, Hangzhou 310027, PR China
[b] SEPCO Electric Power Construction Corporation, Power Construction Corporation of China, PR China

ARTICLE INFO

Keywords:
Low-low temperature economizer system
Capacity expansion retrofit
Waste heat utilization
Flue gas prediction
Real-time optimization

ABSTRACT

This study integrates a low-low temperature economizer (LLTE) into the flue of a 1000 MW supercritical unit and connects a combined air heater in parallel with the existing condensate system. To investigate the impact of this transformation on critical performance indicators such as thermal efficiency, power generation, and coal consumption, two sets of experiments are carried out under different modes. To address the fluctuations in flue gas parameters during actual operation and the considerable lag associated with traditional PID control, which often leads to suboptimal utilization of flue gas waste heat, this study proposes a CPO-LSSVM intelligent vector regression model. This model enables real-time prediction of flue gas temperature (fgt) and flow rate at the inlet of the LLTE. Based on the prediction results, a thermal system optimization model for the LLTE combined with the air heater is developed using HYSYS. Multi-parameter coupling optimization of fgt, air temperature, and water temperature is then performed using the CPO-HYSYS. Specifically, the Mean Absolute Percentage Error of the fgt prediction under Mode A is 0.15 %, while under Mode B is 0.32 %. After optimization, Mode A achieves a coal consumption reduction of 2.81 g/kWh, while Mode B achieves a reduction of 2.51 g/kWh.

1. Background

Since the 21st century, energy conservation, environmental protection, and sustainable development have become primary global concerns. Two significant issues in energy utilization persist: first, although total energy consumption is decreasing, carbon dioxide emissions and environmental pollution due to resource depletion and energy use remain urgent concerns (Muriuki, Wekesa, Njoka, & Management, 2024). By 2040, global energy demand is projected to rise by one-third, with industry and buildings expected to account for over 75 % of this growth. Additionally, global carbon emissions are expected to continue increasing (Tang et al., 2024). Second, energy efficiency remains a challenge. A significant amount of energy is lost as residual heat during the use of primary energy sources. In high-energy-consuming industries, extensive mechanical operations produce substantial amounts of waste heat. When this residual heat is released into the environment, it decreases energy utilization efficiency and contributes to thermal pollution and considerable energy waste (Lu, Lü, Välisuo, Zhang, & Clements-Croome, 2024). Therefore, the recovery and reuse of low-temperature waste heat have become crucial areas of current research (Chen, Wang, Ding, & Li, 2023).

Primary applications of low-temperature waste heat include power generation (Al-Dahidi, Alrbai, Al-Ghussain, & Alahmer, 2024) and refrigeration (Saoud, Bruno, Boukhchanaa, & Fellah, 2023). The Organic Rankine Cycle (ORC) is a prominent example used for power generation (Lee, Chung, Kim, Jeong, & Kim, 2023; Yang & Yeh, 2022). Recent research has concentrated on several aspects, such as simulating mixed refrigerants, optimizing combined cycle systems, analyzing expander characteristics, and investigating ORC experimental features (Wang et al., 2022; Zhang et al., 2023). However, ORC technology is ineffective when the heat source temperature is below 80 °C due to low efficiency (Dong et al., 2021).

Therefore, raising the temperature of lower-grade energy for reuse is a more viable solution. This concept led to the development of heat pump technology (Weitzer et al., 2022). On the one hand, heat pumps

* Corresponding author.
E-mail addresses: Huaanlidayayup@163.com (H. Li), weidl@zju.edu.cn (D. Wei), frey916@foxmail.com (Y. Wu), li.h@sepco.net.cn (H. Li), liu.hongtao@sepco.net.cn (H. Liu), hu.xl@sepco.net.cn (X. Hu), zhang.hx@sepco.net.cn (H. Zhang), zhouhao@zju.edu.cn (H. Zhou).

https://doi.org/10.1016/j.eswa.2025.128352
Received 7 November 2024; Received in revised form 21 May 2025; Accepted 24 May 2025
Available online 3 June 2025

Nomenclature

Symbol

b_0	coal consumption for power generation before the retrofit. g/kWh
$b1$	coal consumption for electricity generation. g/kWh
B_j	coal consumption without correction. kg/s
c	saving CO_2 emission. t/h
H	Enthalpy. kJ/kg
HR	heat consumption rate. %
η	thermal efficiency. %
Q	energy. kW
m	flow rate. kg/s
ΔN	additional work performed by 1 kg of coal. kJ/kg
P	output power. kW
ξ	the carbon dioxide emitted from burning 1 kg of standard coal. kg
V	enthalpy values of 1 m^3. kJ/m^3
n_r	the r-stage extraction efficiency. %
τ_r	condensation water enthalpy rise of the r-stage heater. kJ/kg

Abbreviation

αi	Lagrange multipliers
b	bias term
CPO	Crested Porcupine Optimizer
e_i	regression error
fgt	flue gas temperature
fgit	flue gas inlet temperature
fgot	flue gas outlet temperature
$K(x_i, x_j)$	kernel function
L	Lower bound
LLTE	Low-low temperature economizer
LSSVM	Least Squares Support Vector Machine
N	population size
MAE	Mean Absolute Error
MAPE	Mean Absolute Percentage Error
Mt	The fourth defense mechanism normalizes the fitness
r	random number
RBF	radial basis function
RMSE	Root Mean Square Error
S	the step size
St	The third defense mechanism normalize the fitness
T	cyclic variable
U	Upper bound
w	weight vector
x	solution
τ	random number
γ	regularization parameter
Ω	symmetric matrix
σ	the bandwidth of the kernel function

can increase the temperature of low-grade heat sources for power generation or heating; on the other hand, they can be used for refrigeration. Refrigeration methods include adsorption refrigeration and absorption refrigeration. Silica gel water is a new representative of adsorption refrigeration, while LiBr is a typical example of absorption refrigeration technology (Pan, Peng, Wang, Sun, & Wang, 2019).

Compared to the methods mentioned above, installing an LLTE downstream of the flue offers several advantages, including mature technology, low cost, and ease of implementation (Fan, Pei, Wei, & Management, 2018). Traditional air heaters often rely on more heat sources, such as auxiliary steam, which has high quality and significant power capacity. However, using this steam to heat the boiler's cold secondary air can result in the waste of steam quality, leading to decreased economic efficiency of the unit. Additionally, traditionally used auxiliary steam heaters frequently experience issues such as pipeline vibration or water hammer during operation and shutdown, which can pose safety risks to the equipment. In this context, the technology for utilizing flue gas waste heat (fgwh) has emerged, combining an LLTE with an air heater.

Han et al. (Han et al., 2017) developed a recovery system for the deep utilization of flue gas. The results show that this system can reduce coal consumption by 4.00 g/kWh. Yang et al. (Yang et al., 2015) simulated installing of LLTE for heating condensate water and preheating air in a 1000 MW coal-fired unit. The results indicate that the annual net earnings after the retrofit reached as high as $85.8 million. To deeply utilize fgwh, Stevanovic et al. (Stevanovic et al., 2019) designed a combined system of high- and low-temperature economizers. They analyzed the impact of the economizer installation position on the system power. Yan et al. (Yan et al., 2018) proposed an optimized system combining an LLTE with an air heater to recover fgwh and conducted simulation analysis. The results indicate that the coal consumption is reduced by 5.38 g/kWh after the retrofit. Xu et al. (Xu et al., 2014) suggested an innovative system combining LLTE with an air heater and conducted simulation analysis. The maximum output power can reach 900 MW. Espatolero et al. (Espatolero, Cortés, & Romeo, 2010) took output power and generation cost as objectives and used Aspen software to perform optimization analysis on different layouts of LLTE.

To address the issue of elevated flue gas temperature(fgt) in coal-fired power plants after 30 years of operation, Stevanovic et al. (Stevanovic, Wala, Muszynski, Milic, & Jovanovic, 2014) implemented high-temperature economizers alongside LLTE systems to recover waste heat from the flue gas for preheating heat transfer water and the secondary air. Their results demonstrate that the LLTE approach produces the most significant improvement in thermal efficiency. Xiao et al. (Xiao, Zhang, Wang, & Wang, 2019) introduced a bypass staged LLTE approach. Compared with conventional LLTE, the enhanced LLTE system can further reduce the standard coal consumption rate by 1.1 g/kWh. Ma et al. (Ma et al., 2021)developed a novel WHR system based on LLTE that utilizes LiBr as the working fluid. By leveraging the phase transition of LiBr, the system efficiently recovers waste heat from flue gas and channels it into preheating cold air, thereby significantly enhancing the overall energy utilization efficiency. Xu et al. (Xu, Jin, Zhu, & Li, 2021)constructed a 330 MW LLTE experimental device to evaluate its heat exchange performance and determine optimal input parameters under various operating conditions. Li et al. (Li, Chen, Jiang, & Lu, 2023)developed a comprehensive coal-fired power plant model using Aspen Plus, incorporating a cascade design for flue gas WHR. The new system reduces coal consumption by 3.69 g/kWh and conserves 46.48 t/h of water extracted from the flue gas. Ouyang et al. (Ouyang et al., 2021) introduced an innovative approach utilizing low-temperature flue gas for power generation and sulfuric acid recovery. This system produces 2123 kg/h of sulfuric acid, enhancing the unit's thermal efficiency by 0.64 %. Flue gas bypass technology was applied by Zhang et al. (Zhang, Zhang, Sun, Liu, & Yan, 2024) to heat cold water and secondary air, establishing a fgwh system model. After parameter optimization, the system achieved an exergy efficiency of 49.8 % and reduced coal consumption by 4.75 g/kWh.

Huang et al. (Huang et al., 2024) proposed a fgwh recovery system that couples flue gas bypass with LLTE technology, while also employing a heat pump to preheat the secondary air. The results show that the system can achieve an energy utilization efficiency of up to 44 %, with a total recovered waste heat of 20.845 MW. Han et al. (Han et al., 2021a)

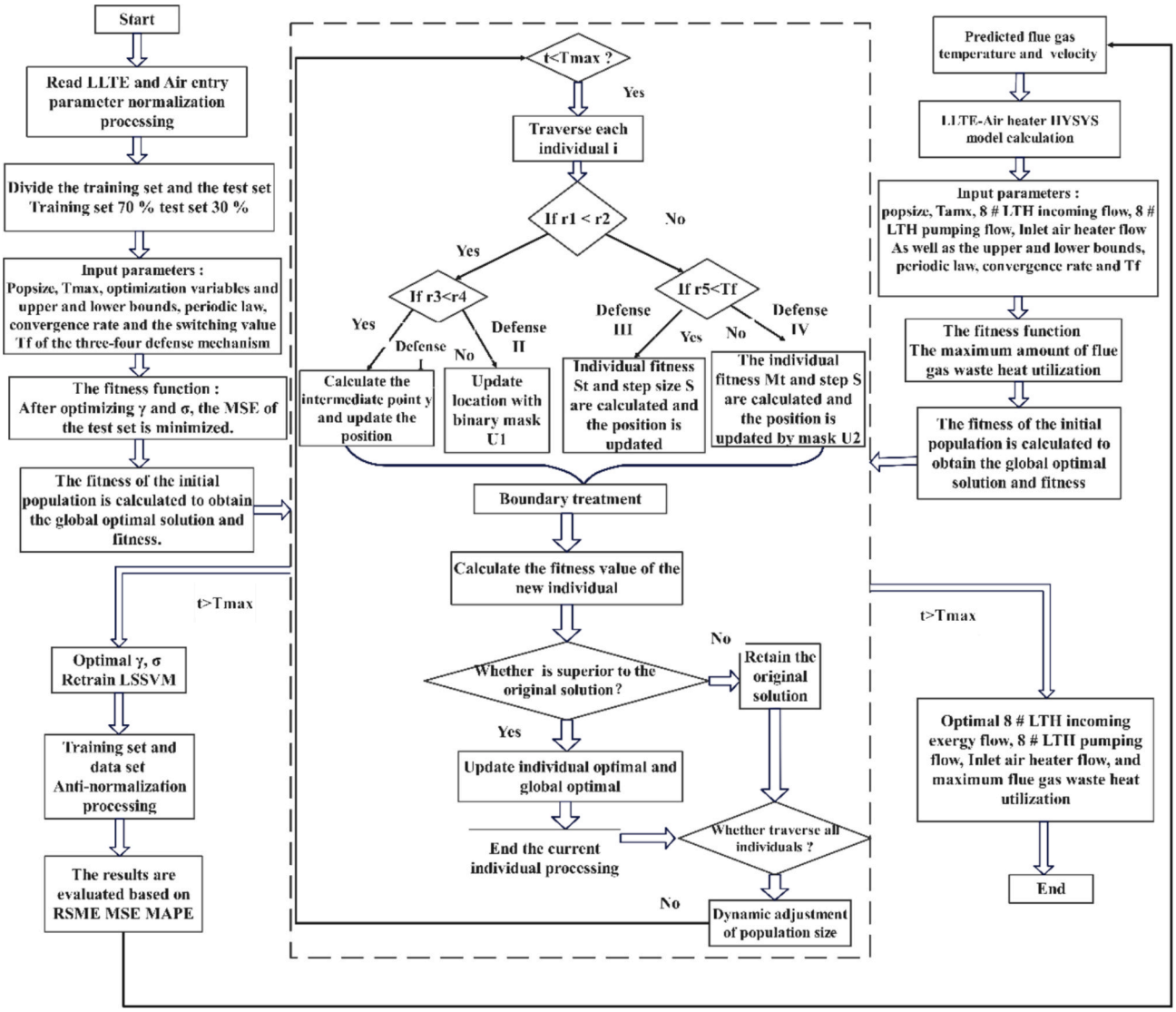

Fig. 1. Algorithm flowcharts of CPO-LSSVM and CPO-HYSYS.

employed a flue gas bypass system coupled with an LLTE to enable cost-effective discharge of flue gas desulfurization wastewater. By using flue gas as the heat source, the treatment cost was reduced by 41.5 %. Tan et al. (Tan et al., 2021) installed two LLTEs upstream and downstream of the desulfurization tower to recover low-temperature fgwh. Under the optimal configuration, the system achieved a coal saving of 4.11 g/kWh. Chantasiriwan et al. (Chantasiriwan, 2021) investigated the optimal installation configuration of LLTEs, secondary air preheaters, and flue gas dryers for biomass boilers. Liu et al. (Liu, Zhao, Wang, Abdulwahid, & Han, 2022) proposed a novel system that couples an LLTE with a CO_2 refrigeration cycle. The system was optimized using a genetic algorithm, and the results showed that the integration of the LLTE improved the COP of the CO_2 refrigeration system.

According to the author's investigation, experimental studies on capacity enhancement retrofits in large-scale power plants are relatively scarce at the current stage of research. Most existing studies rely primarily on simulation models, while the limited experimental research mainly focuses on the impact of introducing a single LLTE device. There is a lack of in-depth exploration of the economic effects of combined LLTE and secondary air heater retrofits in power plant applications.

Moreover, existing studies only assess the benefits following the initial capacity retrofit and typically assume constant flue gas temperature and flow rate. However, in actual engineering operations after LLTE is coupled with a secondary air heater, significant fluctuations in flue gas temperature and flow rate are common. The influence of the heat transfer water distribution ratio between the LLTE and the secondary air heater on fgwh recovery has yet to be studied.

More notably, current capacity retrofit projects still rely on traditional PID control methods to regulate the water flow into the LLTE and the secondary air heater. In actual operations, under variable load conditions, the flue gas–water heat exchange system of the LLTE exhibits pronounced nonlinearity and significant time delays. These characteristics make it difficult for conventional control methods to achieve precise regulation. Therefore, there is an urgent need to adopt intelligent algorithms to address these challenges of delay and fluctuation and further enhance the efficiency of fgwh utilization. Based on this context, the main research work conducted in this study is as follows:

(1) In response to the sharp rise in fuel costs in recent years for a 1000 MW ultra-supercritical unit—leading to a significant deviation between the actual and design coal types and resulting in fgt 3–5 °C higher than the design value during operation—this study investigates a retrofit scheme involving the installation of a LLTE within the flue duct. The LLTE is arranged in parallel with the original condensate system and integrated with the air preheater. Two sets of experimental studies are conducted under different load conditions to examine the impact of the retrofit on key performance indicators, including thermal efficiency,

Table 1
Pseudocode for flue gas parameters prediction based on CPO-LSSVM.

Algorithm 1 Prediction of flue gas temperature and flow rate based on CPO-LSSVM

Input: LLTE inlet and air heater parameters, and boiler parameters
Output: Flue gas Temperature and flow rate
1. Normalized data according to Eq. (28)
2. Define the fitness function for minimizing MSE
2-1. Initializing LSSVM model; configure the model parameters using Eq. (21)
3. CPO optimization regularization parameters$\gamma$and σ
Set parameters *N, Tmax, α, Tf, T, Nmin.*
Initialize the solutions' positions randomly, X^i, i = 1,2.N
3-1. ***While*** ($t < Tmax$)
3-2. Evaluate fitness for each individual
Determine the best solution $\overrightarrow{x_{CP}^t}$
Update the population size using Eq.23
For $i = 1:N$
3–3 Generate two random numbers, r_1 and r_2
If $r_1 < r_2$ %%***Exploration stage***
Generate two random numbers, r_3 and r_4
3–4 **If** $r_3 < r_4$ %%Defense I
Using Eq. (24)
Else %%Defense II
Using Eq. (25)
Else %%***Exploration stage***
Generate random numbers, r_5
If $r_5 < Tf$ %%Defense III
Using Eq. (26)
Else %%Defense IV
Using Eq. (27)
If $f\left(\overrightarrow{x_i^{t+1}}\right) > f\left(\overrightarrow{x_i^t}\right)$
$\overrightarrow{x_i^{t+1}} = \overrightarrow{x_i^t}$
End If
t = t + 1
END for
End while
3-6 **Return** $\overrightarrow{x_{CP}^t}$
4 LSSVM is trained based on$\gamma$and σ
5 Evaluate the flue gas parameters prediction

power output, and coal consumption per unit of electricity generated.

(2) To address the challenges of fluctuation and significant time delays in flue gas parameters during the capacity retrofit's operation, this study employs a CPO-LSSVM intelligent support vector regression model. Based on real-time boiler combustion conditions, the model predicts the inlet flue gas temperature and flow rate of the LLTE, enabling feedforward control. When boiler load changes occur, the system preemptively adjusts valve openings to maintain stable control of fgt, air, and water temperature within the LLTE.

(3) Based on the prediction results, a simulation model of the LLTE coupled with a secondary air heater is developed using HYSYS. The CPO algorithm is then integrated with HYSYS to optimize the distribution ratio of heat transfer water between the LLTE and the secondary air heater, aiming to maximize fgwh recovery during actual operation. The optimization variables included the inlet flow rate of the No. 8 LTH, the extraction water flow rate from the No. 8 LTH, and the heat transfer water flow rate to the air heater. By comparing the experimental and optimized results, changes in key performance indicators such as power output, thermal efficiency, and coal consumption per unit of electricity are analyzed, providing strong support for the efficient operation of power plants after capacity enhancement retrofits.

2. Model

2.1. System analysis

The equivalent enthalpy drop method is based on the thermodynamic principle of heat-work conversion and is used to analyze the efficiency of heat-to-work conversion and energy utilization. To facilitate analysis and comparison, the non-tail flue gas heat utilization system is the benchmark system, with 1 kg of coal as the reference. The unit's internal heat absorption is the adequate heat released by the flue gas from the SCR outlet to the desulfurization absorption tower inlet. Changes in the system's work after transformation are analyzed, and the boiler efficiency of the reform system can be expressed:

$$\eta_g = \eta_{SG} + \Delta\eta_1 \tag{1}$$

Where, η_{SG} represents the baseline boiler efficiency, %; $\Delta\eta_1$ denotes the efficiency gain following modifications, %; and η_g is the updated system efficiency, %.

The thermal efficiency of the boiler can be expressed as:

$$\Delta\eta_1 = \frac{H_{y1} - H_{y2}}{H_{net}} \tag{2}$$

Where, H_{y1} and H_{y2} are the enthalpies of flue gas before and after LLTE, kJ/kg; H_{net} is the coal calorific value, kJ/kg. The additional work performed by 1 kg of coal can be expressed as:

$$\Delta N = (H_{y1} - H_{y2})\eta_{gd}\eta_i - \frac{Q_c}{B_j}(\eta_i - \eta_{jp1}) \tag{3}$$

Q_c refers to the cold medium water reuse of fgwh, kW; B_j is the coal consumption without correction, kg/s; η_i is the efficiency of the turbine without retrofit, %.η_{jpl} refers to the average extraction efficiency, %; η_{gd} represents the pipeline efficiency, %.

The increase in thermal efficiency after transformation is as follows:

$$\delta\eta_1 = \frac{(H_{y1} - H_{y2})\eta_{gd}\eta_i - \frac{Q_c}{B_j}(\eta_i - \eta_{jp1})}{H_{net}\eta_{SG1}\eta_{gd}\eta_i - \frac{Q_c}{B_j}(\eta_i - \eta_{jp1})} \tag{4}$$

According to the theory of equivalent enthalpy drop, the average heat utilization efficiency of the 7 # LTE economizer is:

$$\eta_{jp1} = \frac{(h_{c1} - h_m)\eta_{m-1} + \sum_{r=m}^{n}\tau_r n_r}{(h_{c1} - h_m) + \sum_{r=m}^{n}\tau_r} \tag{5}$$

After transformation, the economizer in the system is typically configured in parallel. The enthalpy of the condensate and feed water at the outlet of each economizer should be equal to the enthalpy of the working fluid at the outlet of the heater at that level in the system, so $h_{c1} = h_m$. From the above equation, η_{jp1} can be derived as:

$$\eta_{jp1} = \frac{\sum_{r=m}^{n}\tau_r n_r}{\sum_{r=m}^{n}\tau_r} \tag{6}$$

In the above formula, h_{c1} is the condensate water enthalpy at the outlet of the reformed economizer, kJ/kg;h_m is the m-stage heater outlet enthalpy, kJ/kg; η_{m-1} is the extraction efficiency of m-1 level in the reformed system, %; τ_r is the condensation water enthalpy rise of the r-stage heater, kJ/kg; n_r is the r-stage extraction efficiency, %.

2.2. Thermodynamic analysis

The utilization of fgwh can be expressed as:

$$Q_c = m_1(h_2 - h_1) \tag{7}$$

m_1 is the heat medium water flow rate, kg/s; h_1 and h_2 represent the water enthalpies at the inlet and outlet of the LLTE, kJ/kg.

For air heaters, the absorbed heat can be expressed as:

$$Q_f = m_2(h_4 - h_3) \tag{8}$$

Among them, m_2 is the airflow rate entering the air heater system, kg/s; h_4 and h_3 represent the enthalpies at the inlet and outlet of the air heater, kJ/kg;

Exergy can reflect the availability of energy and is more effective than energy [32], and it can be expressed as:

$$e = h_i - h_0 - T_0(s_i - s_0) \tag{9}$$

Table 2
Pseudocode for CPO-HYSYS optimization of LLTE-air heater parameters.

Algorithm 2 CPO-HYSYS Optimizes LLTE-Air Heater Parameters

Input: fht and flow rate via CPO-LSSVM
Output: 8#LTH incoming flow, 8#LTH pumping flow, Inlet air heater flow, the maximum amount of fgwh utilization
1. Read the fgt, and flow rate and real-time experimental parameters are introduced into the LLTE-Air Heater model
2. Define the fitness function as the maximum amount of fgwh utilization
3. CPO optimizes 8# LTH incoming flow, 8# LTH pumping flow, and Inlet air heater flow to maximize the utilization rate of fgwh
Set parameters *N, Tmax, α, Tf, T, Nmin.*
Initialize the solutions' positions randomly, X^i, i = 1,2.N
3-1 ***While*** ($t < Tmax$)
3-2 Evaluate fitness for each individual
Determine the best solution $\overrightarrow{x_{CP}^t}$
Update the population size using Eq.23
For $i = 1{:}N$
3–3 Generate two random numbers, r_1 and r_2
If $r_1 < r_2$ %%***Exploration stage***
Generate two random numbers, r_3 and r_4
3–4 **If** $r_3 < r_4$ %%Defense I
Using Eq. (24)
Else %%Defense II
Using Eq. (25)
Else %%***Exploration stage***
Generate random numbers, r_5
If $r_5 < Tf$ %%Defense III
Using Eq. (26)
Else %%Defense IV
Using Eq. (27)
If $f\left(\overrightarrow{x_i^{t+1}}\right) > f\left(\overrightarrow{x_i^t}\right)$
$\overrightarrow{x_i^{t+1}} = x_i^t$
End If
t = t + 1
END for
End while
3-6 **Return** $\overrightarrow{x_{CP}^t}$
4. Output maximum fgwh utilization, 8#LTH incoming flow, 8#LTH pumping flow, Inlet air heater flow

s represents the entropy, kJ/(kg·K).

The analysis of the LLTE and the air heater is:

$$\sum m_{in}e_{in} + E_q = \sum m_{out}e_{out} + E_L \tag{10}$$

$\sum m_{in}e_{in}$ is the energy at the inlet of coolant water, kW; E_q is the energy at the inlet of the heater or economizer, kW; $\sum m_{out}e_{out}$ represents the energy of the heat medium water at the outlet, kW; E_L denotes the outlet energy of the air heater or economizer, kW.

2.3. Economic analysis

The unit's total heat consumption is determined from its heat balance, and the measured heat consumption rate is derived by integrating the electric power data, it can be shown as:

$$HR = \frac{G_{MS} \times H_{MS} + G_{HRH} \times H_{HRH} - G_{FW} \times H_{FW} - G_{CRH} \times H_{CRH} - G_{YEJ} \times H_{YEJ} - G_{RH} \times H_{RH}}{P_G} \tag{11}$$

P_G is the output power, kW; G_{MS} and H_{MS} is the primary steam flow rate and enthalpy, in t/h and kJ/kg; G_{HRH} and H_{HRH} are the reheat steam flow rate and enthalpy, in t/h and kJ/kg; G_{FW} and H_{FW} are the feedwater flow rate and enthalpy, in t/h and kJ/kg; G_{CRH} and H_{CRH} are the cold reheated steam flow rate and enthalpy, in t/h and kJ/kg; G_{YFJ} and H_{YFJ} are the induced draft fan steam flow rate and enthalpy, in t/h and kJ/kg;G_{RH} and H_{RH} are the desuperheating water flow rate and enthalpy, in t/h and kJ/kg.

The coal consumption for electricity generation is defined as:

$$b1 = \frac{HR}{Q_c \times \eta_{gd} \times (1 - c) \times \eta_g} \tag{12}$$

The reduction in coal consumption is defined as:

$$\Delta b = b0 \times \delta\eta_1 \tag{13}$$

b_0 represents the coal consumption for power generation before the retrofit, g/kWh.

Installing LLTE can reduce fuel and water consumption and pollutant emissions. The saving of CO_2 emissions is:

$$c = \frac{\xi \times \Delta b \times P}{1,000,000} \tag{14}$$

Where, ξ is the carbon dioxide emitted from burning 1 kg of standard coal, kg; P is the output power, kW.

2.4. LSSVM model

LSSVM is an effective regression method that combines least squares and SVM theory, offering better generalization capability than traditional least squares methods. A nonlinear function φ(xi) transforms the input space into the feature space. The form of the model is as follows:

$$f(x) = b + \langle \phi(x), w \rangle \tag{15}$$

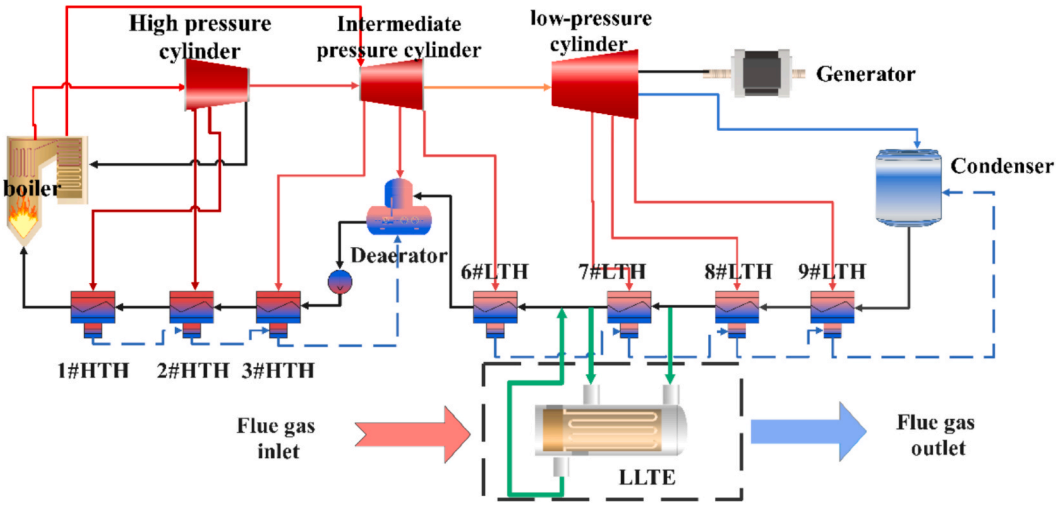

Fig. 2. Capacity-increasing transformation scheme.

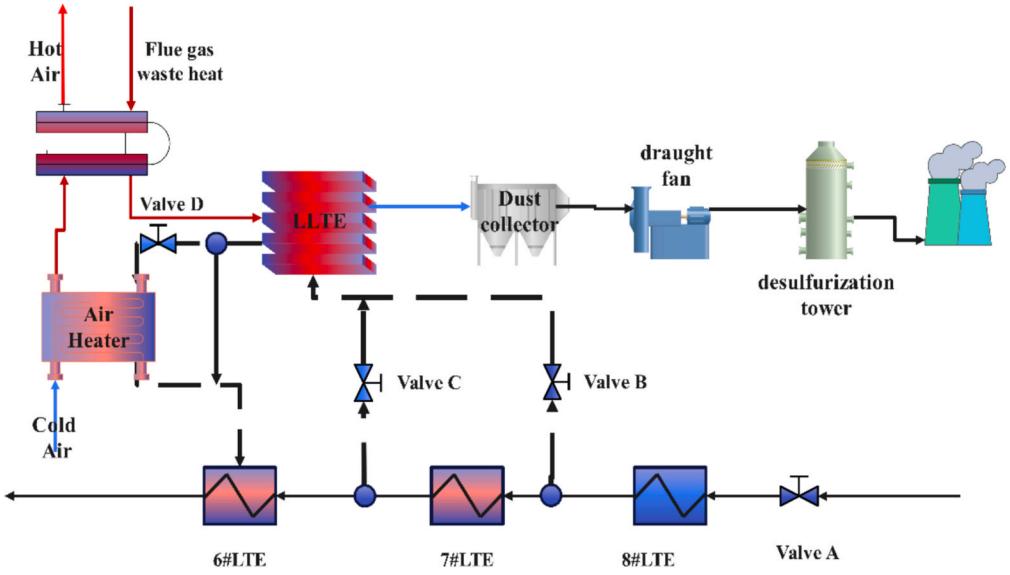

Fig. 3. Schematic diagram of LLTE combined with secondary air heater.

w represents the weight vector, and b denotes the bias term. The evaluation issue is an optimization problem

$$\begin{aligned} &minJ(w,e) = min\left(\frac{1}{2}\|\boldsymbol{w}\|^2 + \frac{1}{2}\gamma\sum_{i=1}^{N} e_i^2\right) \\ &s.t.y_i = \langle \boldsymbol{w}, \phi(\boldsymbol{x}_i)\rangle + b + e_i i = 1,2,\cdots,N \\ &\gamma > 0 \end{aligned} \tag{16}$$

γ is the regularization parameter that helps balance the trade-off between the complexity of the model and its accuracy, while e_i signifies the regression error between the actual and predicted output values. To solve the above optimization problem, the corresponding Lagrangian function is constructed:

$$L_{\text{LSSVM}} = \frac{1}{2}\|\boldsymbol{w}\|^2 + \frac{1}{2}\gamma\sum_{i=1}^{N} e_i^2 - \sum_{i=1}^{N}\alpha_i\{\langle \boldsymbol{w}, \phi(\boldsymbol{x}_i)\rangle + b + e_i - y_i\} \tag{17}$$

αi denotes the Lagrange multipliers. By removing w and ei, the four linear problems are as follows:

Table 3
Performance parameters of single LLTE in the design conditions.

LLTE performance parameters	Type/Specification
Flue gas volume	3184970 Nm^3/h
Inlet fgt	176 °C
Outlet fgt	90 °C
Inlet mixed water temperature	70 °C
Outlet mixed water temperature	87 °C
absorbed heat	40300 kW

Table 4
LLTE structural parameters.

LLTE structure parameters	6(7 m × 7 m × 6.5 m)
Direction	Horizontal flow
Pressure drops	0.15 MPa/The water side pressure of the LLTE, heater, and piping system is about 0.5 MPa
Heat exchanger	H-type finned tube, in series Outer diameter: 38.1 mm; Wall thickness: 4 mm Fin thickness: 2 mm
Heat exchanger material	ND Steel
Heat exchange area	110000 m^2

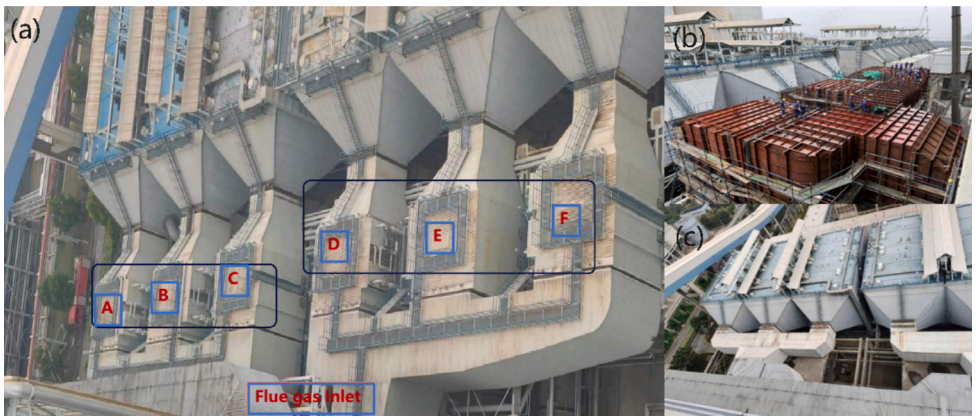

Fig. 4. Experimental device of LLTE.

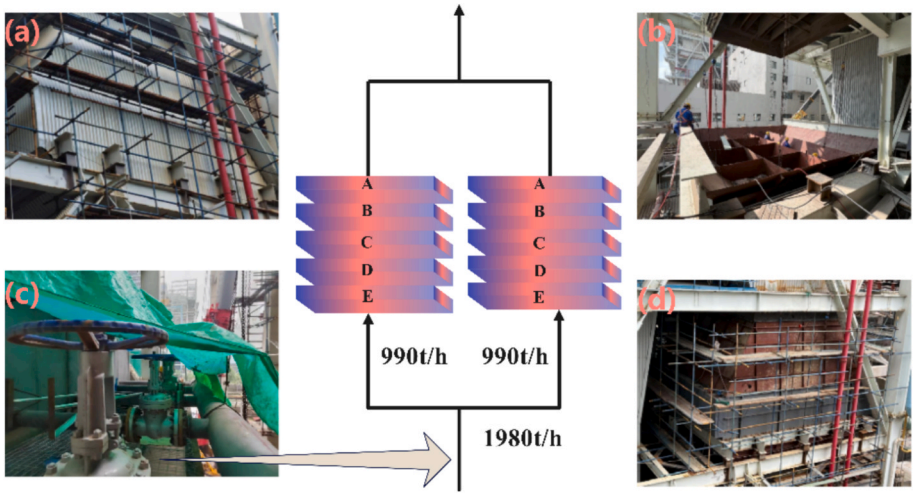

Fig. 5. Air heater experimental device (a) installation of external protection plate (b) flow control valve of inlet air heater (c) installation of guide plate (d) heater module.

Table 5
Air heater performance parameters in design conditions.

Performance parameter	Type/specification
air volume	2253271 Nm^3/h
inlet air temperature	20 °C
outlet air temperature	100 °C
Inlet water temperature	117 °C
Outlet water temperature	87 °C
water inflow	1980 t/h
Heat exchanger material	20G + AL, base tube carbon steel, fin aluminum

$$\begin{bmatrix} 0 & E^{T} \\ E & \Omega+\frac{1}{\gamma}E \end{bmatrix}\begin{bmatrix} b \\ \alpha \end{bmatrix}=\begin{bmatrix} 0 \\ y \end{bmatrix} \tag{18}$$

Here, $y=[y_1,\ldots,y_n]^T$, $\alpha=[\alpha_1,\ldots,\alpha_n]^T$, and $E=[1,\ldots,1]^T$. Ω represents an $N\times N$ symmetric matrix of the kernel function.

$$\Omega_{ij}=K(x_i,x_j)=\phi(x_i)^T\phi(x_j)i,j=1,2,\cdots,N \tag{19}$$

$K(x_i,x_j)$ is the kernel function that meets the Mercer condition, and the LSSVM model is as follows:

$$y(x)=\sum_{i=1}^{n}\alpha_iK(x_i,x)+b \tag{20}$$

LSSVM demonstrates good performance in handling regression problems. However, selecting an appropriate kernel function remains crucial in applying LSSVM. The radial basis function can be expressed as follows:

Table 6
Structure parameters of the air heater.

Structural parameter	2/(10 × 7.75 × 3.24)
direction	horizontal flow
pressure drop	800 Pa/The water-side pressure drop of the air heater is 0.25 MPa.
Heat exchanger form	Spiral finned tube, staggered Outer diameter: 25 mm; wall thickness: 3 mm
Heat exchange area	60000 m^2
installation weight	85 t*2
Total heat absorption	67000kw

$$K(x_i,x_j)=\exp\left(-\frac{\|x_i-x_j\|^2}{2\sigma^2}\right),\sigma>0 \tag{21}$$

σ is the bandwidth of the kernel function.

2.5. CPO optimization algorithm

Like other population-based metaheuristic methods, CPO starts its search with an initial population of individuals:

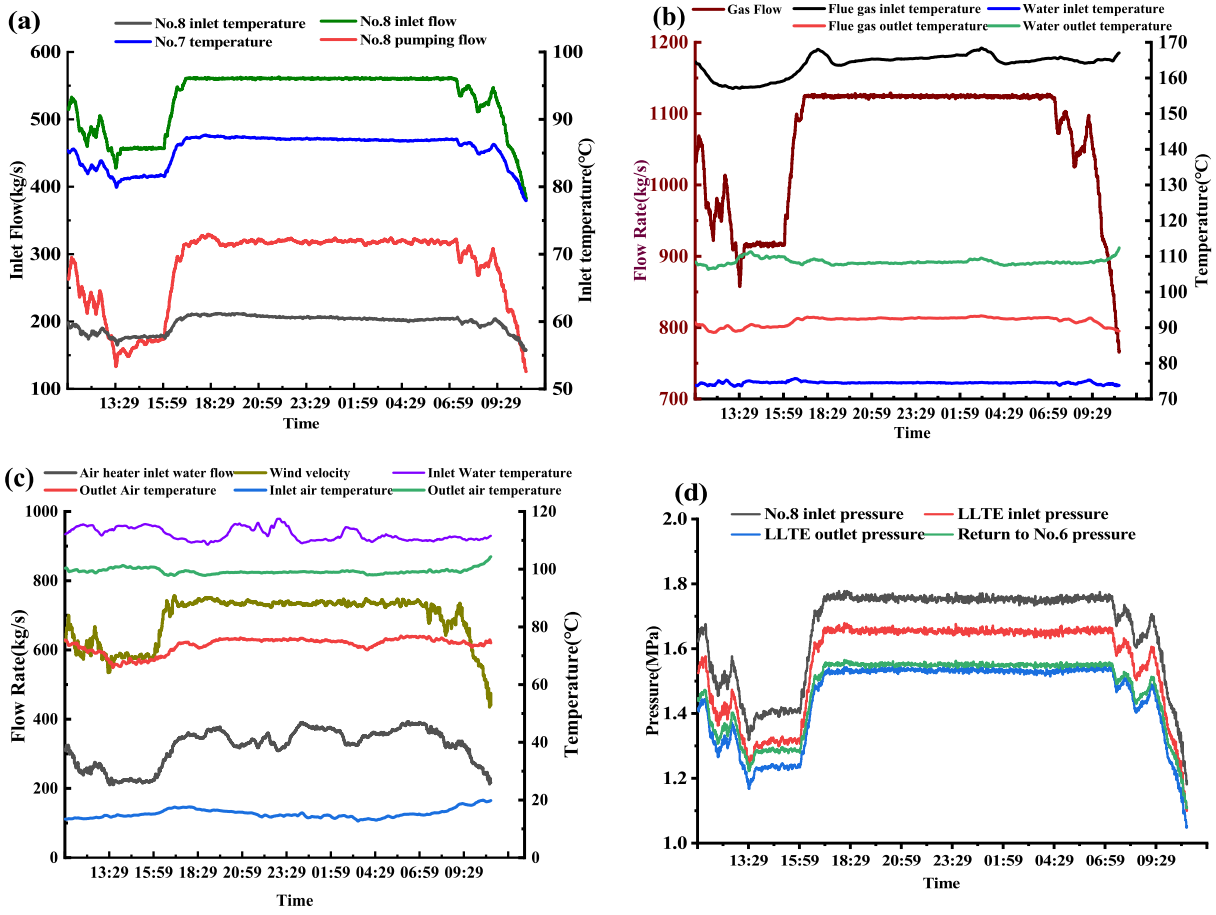

Fig. 6. Real-time change diagram of system parameters of mode A.

$$\overrightarrow{X}_i = \overrightarrow{L} + \overrightarrow{r} \times \left(\overrightarrow{U} - \overrightarrow{L}\right) \Big| i = 1, 2..., N \tag{22}$$

L and U are the lower and upper bounds, N represents the population size, X_i is the i candidate solution, and r is a random number. The algorithm employs a population reduction technique to maintain diversity within the population and accelerate the convergence speed.

$$N = N_{min} + (N - N_{min}) \times \left(1 - \left(\frac{t\%\frac{T_{max}}{T}}{\frac{T_{max}}{T}}\right)\right) \tag{23}$$

T is the variable that determines the number of iterations. t refers to current function evaluation. T_{max} is the maximum number of evaluations allowed. % represents the remainder, and N_{min} is the lower bound of the population.

Defense strategy I is:

$$\overrightarrow{x_i^{t+1}} = \overrightarrow{x_i^t} + \tau_1 \times \left|2 \times \tau_2 \times \overrightarrow{x_{CP}^t} - \overrightarrow{y_i^t}\right| \tag{24}$$

x_{CP}^t is the optimal solution evaluated at iteration t, y_i^t is the vector generated between the current CP and a randomly selected CP from the population, τ_1 is a random number based on a normal distribution, and τ_2 is a random value that falls within the range of [0,1].

Defense strategy II is:

$$\overrightarrow{x_i^{t+1}} = \left(1 - \overrightarrow{U_1}\right) \times \overrightarrow{x_i^t} + \overrightarrow{U_1} \times \left(\overrightarrow{y} + \tau_3 \times \left(\overrightarrow{x_{r1}^t} - \overrightarrow{x_{r2}^t}\right)\right) \tag{25}$$

r_1 and r_2 are random numbers between [1, N], and τ_3 is a random between [0, 1].

Defense strategy III is:

$$\overrightarrow{x_i^{t+1}} = \left(1 - \overrightarrow{U_1}\right) \times \overrightarrow{x_i^t} + \overrightarrow{U_1} \times \left(\overrightarrow{x_{r_1}^t} + S_i^t \times \left(\overrightarrow{x_{r_2}^t} - \overrightarrow{x_{r_3}^t}\right) - \tau_3 \times \overrightarrow{\delta} \times \gamma_t \times S_i^t\right) \tag{26}$$

r_3 and τ_3 are random values, δ is a parameter that governs the search direction, x_i^t is the position, γ_t is the defense factor, and S_i^t is the scent diffusion factor.

Defense strategy IV is:

$$\overrightarrow{x_i^{t+1}} = \overrightarrow{x_{CP}^t} + (\alpha(1 - \tau_4) + \tau_4) \times \left(\delta \times \overrightarrow{x_{CP}^t} - \overrightarrow{x_i^t}\right) - \tau_5 \times \delta \times \gamma_t \times \overrightarrow{F_i^t} \tag{27}$$

x_{CP}^t is the obtained optimal solution, x_i^t represents the i individual at iteration t, α is the convergence speed factor, τ_4 is a random value, and F_i^t is represents the average force applied to the i predator by the CP.

Fig. 1 illustrates the algorithm flowcharts of both CPO-LSSVM and CPO-HYSYS. When applying the CPO-LSSVM approach to predict fgt, the experimentally measured data are first input into the system. The data are then preprocessed to establish the input–output mapping relationship. The time series data are transformed into a sliding window format to support the training of the time-series prediction model. Next, input and output data are normalized, and the dataset is divided into training and testing sets, with 70 % of the data used for training and the remaining 30 % for prediction.

In the application of the LSSVM model, the type of kernel function and the selection of its associated parameters are critical factors that determine the accuracy of the resulting model. Currently, there is no universally accepted method for choosing the optimal kernel function. However, extensive experiments and studies have shown that the Gaussian Radial Basis Function (RBF) kernel exhibits strong adaptability

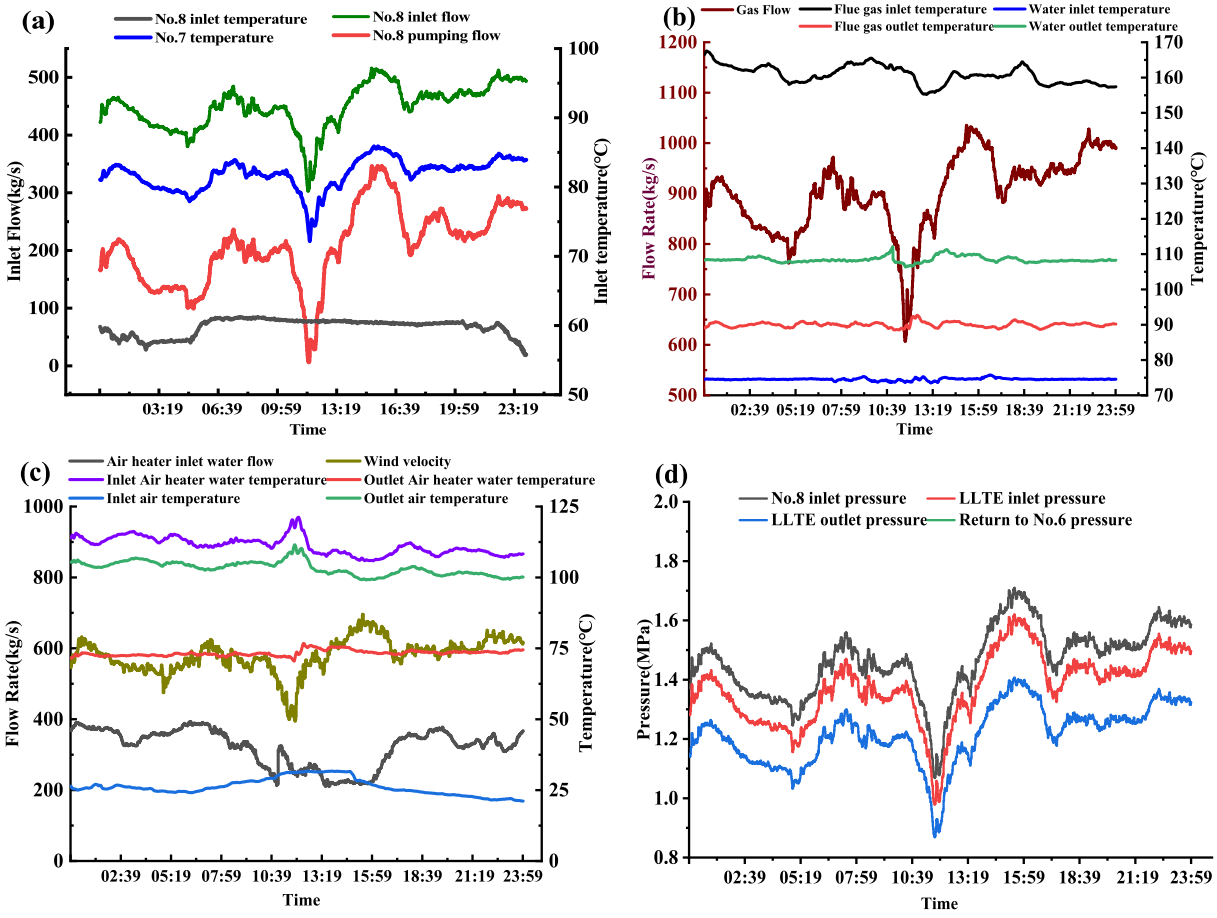

Fig. 7. Real-time changes of system parameters in Mode B.

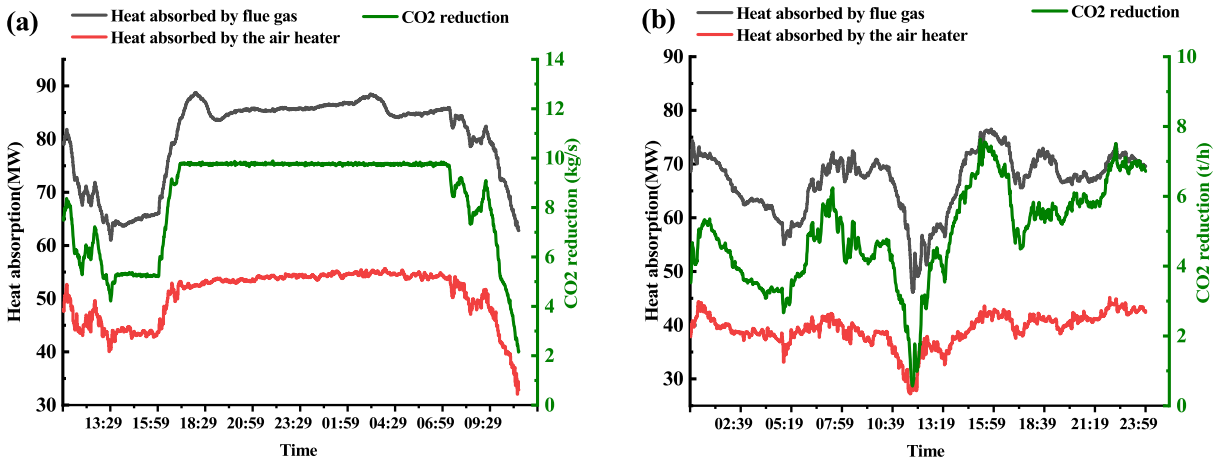

Fig. 8. Analysis of waste heat utilization and emission reduction.

and performance across various scenarios. Therefore, this study adopts the RBF kernel to predict flue gas flow and temperature.

Modeling with the RBF kernel requires specifying appropriate values for the regularization parameter γ and σ, which significantly influence the learning capacity and generalization performance of the LSSVM model. Optimizing these two parameters is essential to constructing an accurate predictive model.

Accordingly, the CPO algorithm is employed to optimize the LSSVM model by setting the population size, maximum number of iterations, and the upper and lower bounds for γ and σ. A customized fitness function is defined to evaluate the quality of each solution by calculating the prediction performance of the LSSVM. The CPO algorithm then searches for the optimal values of γ and σ, returning the best fitness score. The LSSVM model is retrained using the optimized parameters, and the predictions on both the training and testing sets are inverse-normalized before performance evaluation is conducted.

The CPO algorithm incorporates four defense mechanisms. In the first layer, the midpoint between the current individual and a randomly selected individual is calculated to guide the direction of subsequent position updates. To prevent premature convergence to a local optimum,

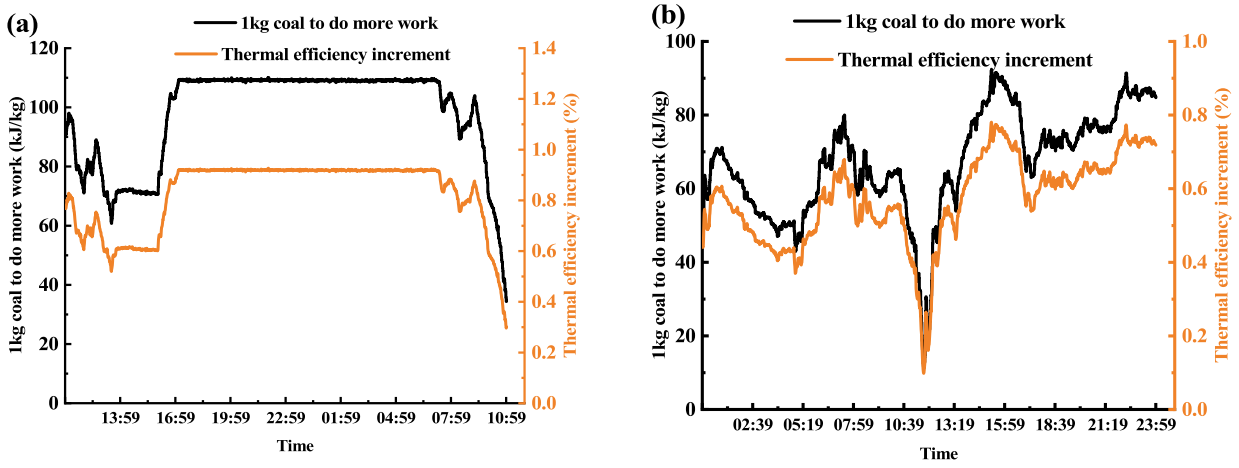

Fig. 9. Changes in heat efficiency and work output.

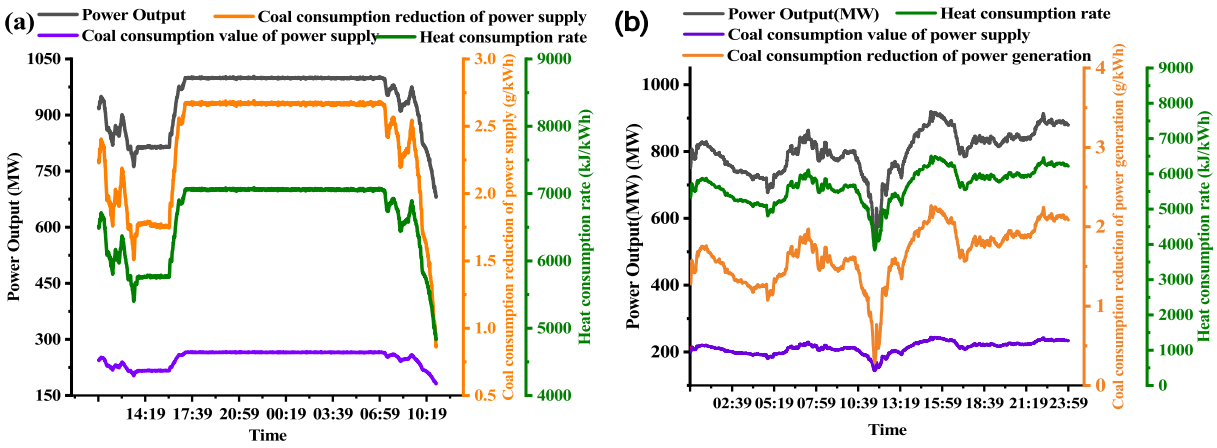

Fig. 10. Economic analysis.

a perturbation-based position update is then performed. Specifically, the current individual is moved toward the differential region between the best global perturbation direction and the random individual's midpoint direction, as described in Eq. (24).

The second defense mechanism represents the core operation of the exploration phase. It begins by computing the midpoint between the current and randomly selected individuals to establish a reference direction for the subsequent hybrid update. A binary mask U1 is then generated for each individual in the population. This mask is used to retain historical information in certain dimensions, helping to maintain population stability: dimensions where the mask equals 1 preserve their current values, while those with a value of 0 undergo exploratory updates to enhance search diversity, as shown in Eq. (25).

During the update, a perturbation term is introduced. Specifically, two distinct individuals are randomly selected, and their difference defines a stochastic exploratory direction. The midpoint offers local guidance, while including a random individual introduces global exploration capability. This design enables the algorithm to maintain stability in selected dimensions while performing guided random exploration in others, effectively balancing the trade-off between exploitation and exploration throughout the search process.

The third defense mechanism begins by normalizing the current individual's fitness relative to the total population fitness (St). An exponential function is introduced in the calculation of St to emphasize the influence of superior individuals. When the optimization target approaches the optimum, a larger St ensures that elite individuals play a dominant role in guiding the search.

At the same time, the step size (S) is adaptively adjusted during the search process. S decays with iterations, allowing more substantial perturbations in the early stages and gradually weaker ones in later stages. This design supports broad exploration in the early phase and fine-tuned exploitation in the later phase. Position updates are performed according to Eq. (26): a binary mask U1 is used to preserve historical information in certain dimensions—dimensions with a mask value of 0 retain their current values, while those with a value of 1 are updated.

The fourth defense mechanism normalizes the fitness of the current individual as a proportion of the total population fitness, denoted as Mt, and applies an exponential function to amplify the weight of superior individuals. After determining the current individual's position, a randomly selected individual is introduced to prevent search pattern stagnation and enhance population diversity.

A directional movement vector is calculated between the current and random individuals. This vector is weighted by Mt, thereby strengthening the attractive pull of high-performing individuals. Additionally, the step size is adaptively adjusted during this process. As shown in Eq. (27), the position is updated by moving the optimal solution toward the global best direction, achieving a balance between rapid convergence and fine-grained local search in the later stages of the algorithm.

Based on the flue gas parameter predictions obtained from the CPO-LSSVM model, the results are fed into the HYSYS simulation in real time. The CPO algorithm defines the population size and number of iterations. The variables 8# LTH incoming flow, 8# LTH pumping flow, and inlet air heater flow are selected as independent variables, with specified

Table 7
Unit Operating Parameters.

Index number	Characteristic	Index number	Characteristic
1	Air Heater Outlet Temperature	20	1th Corner SOFA Valve Position
2	Instantaneous Total Coal Amount	21	2th Corner SOFA Valve Position
3	total airflow	23	3th Corner SOFA Valve Position
4	Primary air volume	24	4th Corner SOFA Valve Position
5	Primary air pressure	25	Primary Superheater Outlet Flow
6	secondary airflow	26	Primary Desuperheater Inlet Temperature
7	Layer A auxiliary air	27	Primary Desuperheater Outlet Temperature
8	Layer A fuel air	28	Tertiary Superheater Outlet Pressure
9	Layer A oil secondary air	29	Secondary Desuperheater Inlet Temperature
10	Layer A bias secondary air	30	Secondary Desuperheater Outlet Temperature
11	Layer B auxiliary air	31	Tertiary Superheater Outlet Temperature
12	Layer B fuel air	32	Reheater desuperheater inlet temperature
13	Layer B oil secondary air	33	Reheater desuperheater outlet temperature
14	Layer B bias secondary air	34	Secondary reheater outlet temperature
15	Layer C auxiliary air	35	Secondary reheater outlet pressure
16	Layer C fuel air	36	6# LTH backwater temperature
17	Layer C oil secondary air	37	Generator power
18	Layer C bias secondary air	38	LLTE inlet fgt
19	furnace pressure		

upper and lower bounds. The optimization is conducted with the objective of maximizing the recovery of fgwh.

The pseudocode for the CPO-LSSVM and CPO-HYSYS algorithms is presented as follows: (Table 1. Table 2).

3. Experimental system

3.1. System description

In this experiment, based on a 1000 MW thermal power unit, the LLTE combined with a secondary air heater system is reformed. It is suggested that the nameplate power of the unit should be increased from 1000 MW to 1055 MW. The transformation plan is shown in Fig. 2.

The system uses water as the heat carrier and recovers the fgwh by passing it through the LLTE and the air heater. A portion of this recovered heat is transferred to the cold air entering the air preheater, while the remaining heat is directed to the thermal system on the steam turbine side. The specific transformation method is illustrated in Fig. 2. Based on operational experience, the boiler's fgt is lower under low load conditions or during startup, and it decreases even further in winter due to lower ambient temperatures. At this time, the fgwh is not only small in value, but too-low fgt will also threaten the heating surface of the cold end of the air preheater.

The primary role of the air heater is to utilize the heat source to warm up the air supplied to the boiler. After the air is heated at the fan outlet, it enters the air preheater for further heating before finally entering the furnace. Research indicates that in regions and seasons with low ambient temperatures, the proper use of air heaters can enhance boiler combustion efficiency and improve the overall operational economy of the unit.

The retrofit scheme plans to extract the incoming flow from the No. 8 low-temperature heaters (LTE) and the incoming flow from the No. 7 LTE into the LLTE. The heated medium water is then directed to the air heater, which preheats the secondary cold air to 100 °C before returning to the No. 6 LTE. After the secondary cold air is preheated to 100 °C. it returns to the No.6 LTE. The energy-saving effect of the LLTE combined air heater system is mainly reflected in the utilization of fgwh, the replacement of the auxiliary steam consumption of the original air heater, and the increase of the air preheater inlet temperature to improve the thermal efficiency of the boiler. LLTE absorbs fgwh to heat the cold air, improve the operating environment of the air preheater, and promote the boiler efficiency (Han et al., 2021b).

3.2. LLTE

In the transformation, each LLTE is arranged in multiple rows aligned with the gas flow direction. Each column must be assembled on-site in groups according to the module to facilitate installation. Each module features an independent inlet and outlet header. The elbow and header are positioned outside the flue, with no intermediate but welding required for the tube bundle pipes. Manual isolation doors and exhaust valves are installed in the headers of each heat exchanger module group, aligned with the flue gas flow direction. This configuration allows for convenient isolation and equipment replacement in the event of a failure. According to Formula 18, the flue gas outlet temperature(fgot)of the LLTE should be between 88 °C and 92 °C under all load conditions.

LLTE features an anti-wear, anti-leakage, anti-corrosion, anti-blocking, and durability design. The heat exchange tubes and fins are made from ND steel, and an H-type finned tube configuration is employed. Each unit includes three rows of false tubes to enhance wear resistance. The wall thickness of the first three rows of heat exchange tubes is at least 5 mm, while the remaining tubes have a minimum thickness of 4 mm. With an annual corrosion rate of less than 0.1 mm, the heat exchange tubes are designed to have a service life exceeding 15 years, accounting for a corrosion allowance of 1 mm. The H-type fins have a minimum thickness of 2 mm, and the fin pitch exceeds 20 mm. They are securely welded to the pipes, with the bonding area exceeding 95 %, ensuring no shedding during transportation or installation. Additionally, the fins at the brackets and edges must be intact to prevent localized wear. The safety valve should be set on the condensate pipe of the LLTE outlet, and ND steel should be selected for the LLTE pipe row and fins. The corrosion rate of ND steel is less than 8 mg/cm^2h^{-1} after being immersed in 50 % sulfuric acid at 70 °C for 24 h. The specific experimental device is shown in Fig. 3.

After entering the LLTE, the flue gas is divided into two streams, containing six parts: A, B, and C, which are one stream, and the other contains D, E, and F. The performance parameters and structural parameters of each part are shown in the following tables (Table 3. Table 4. Fig. 4).

3.3. Air heater

The secondary air heater is designed to have an outlet air temperature of 100 °C. This temperature can be regulated by adjusting the water flow into the secondary air heater. When the operation requires lowering the outlet air temperature, the bypass valve of the secondary air heater should be opened in time to reduce the flow entering the secondary air heater. The specific installation method and parameters of the air heater are shown in the following tables and Fig. 5.

Fig. 5 illustrates the experimental setup of the modified air heater. The secondary air heater is arranged in five modules along the height direction, labeled from top to bottom as A, B, C, D, and E. The heater's performance and structural parameters are detailed in the following tables (Table 5. Table 6).

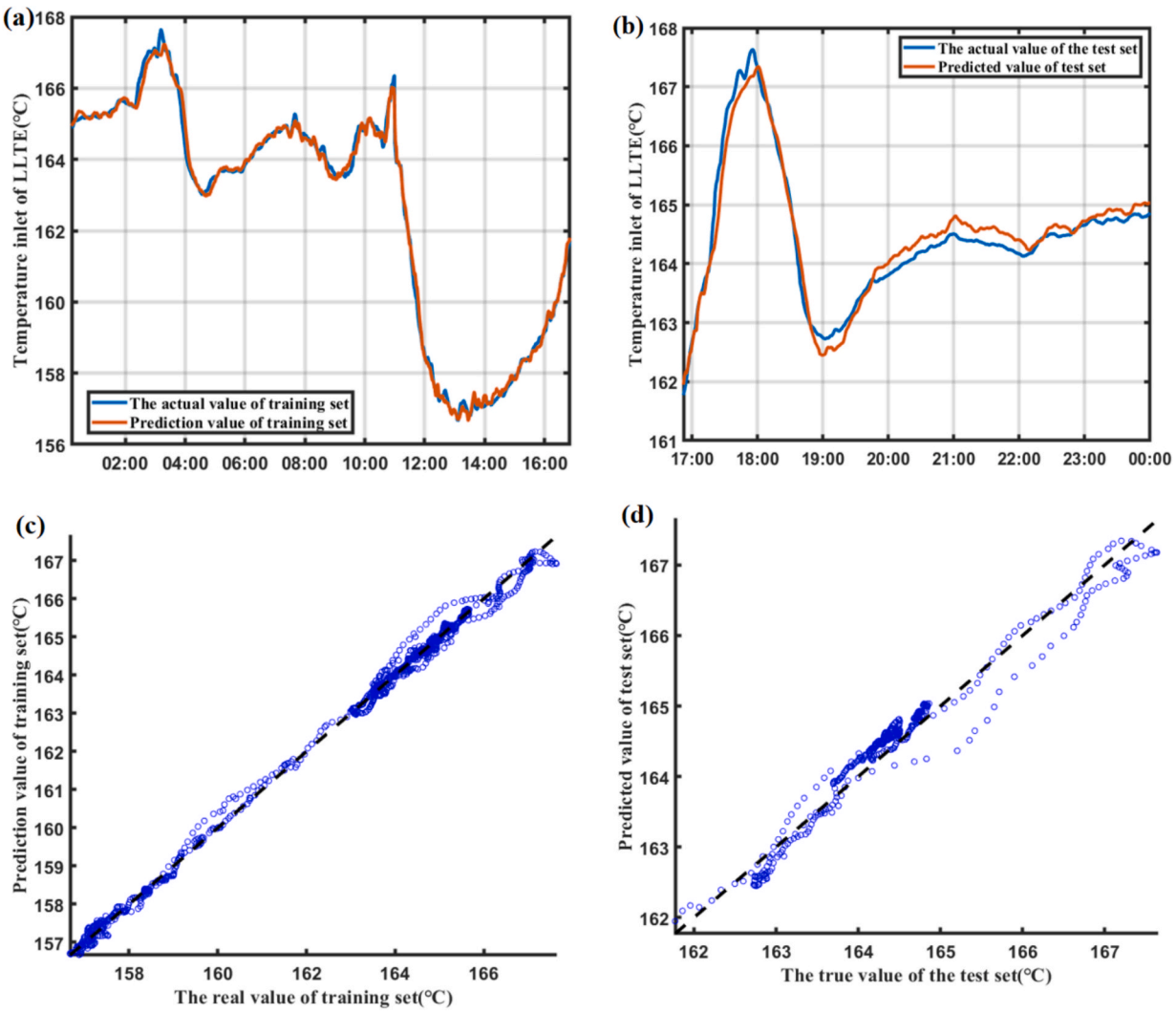

Fig. 11. Prediction of Fgt in Mode A.

4. Experimental study

Based on the experimental device described in Chapter 3, this section conducts experimental research under two different operating conditions and examines the system's performance following capacity expansion. Mode A operates within a power range of 680.27 MW to 1003.23 MW, while Mode B operates from 530.15 MW to 920.15 MW.

Fig. 6 shows the real-time changes in system pressure, flow, and temperature after system capacity expansion and transformation. At 13:30, each parameter reaches its lowest value. The No. 8 inlet flow is divided into two streams, one flowing into the 7# LTE and the other into the LLTE. During the experiment, the valve after the 7# LTE is fully open, and the pumping flow is maintained at around 230 kg/s, resulting in similar trends for the three flow rates. Correspondingly, in subfigure b, the gas flow decreases from 1069 kg/s to 857 kg/s. In subfigure c, the heat medium water flow rate into the heater decreases from 325 kg/s to 210 kg/s, and the wind velocity falls from 700 kg/s to 535 kg/s. In subfigure d, the No. 8 inlet pressure decreases from 1.67 MPa to 1.45 MPa, and the LLTE inlet pressure drops from 1.57 MPa to 1.36 MPa.

Fig. 7 shows the real-time changes in system operating parameters under mode B. As seen from subfigure (a), the incoming flow temperature of No. 8 #LTE is maintained at around 60 °C, and its inlet flow, pressure into LLTE, and flow rate all show the same change trend. At 12:40, it shows a downward trend, mainly due to the reduction in power demand. Among them, the maximum fgt in subfigure (b) is 167.5 °C. At 12:40, it suddenly drops to 155.2 °C. The corresponding change law is directly reflected in the gas flow in (b), the air flow in (c), and the pressure in (d). The average temperature of the heat medium water entering the LLTE is 73.3°C, while the outlet is 111.21°C. The average inlet air temperature of the heater is 26.23°C, while the average outlet air temperature is 103.32°C.

Fig. 8 illustrates the real-time variations in waste heat utilization and CO_2 emission reduction. (a) depicts Mode A, while (b) is Mode B. In Mode A, these parameters experience significant fluctuations between 11:00 and 18:00. Specifically, they fluctuate and decrease between 11:00 and 13:30, followed by a gradual increase from 13:30 to 16:00. At 13:30, the flue gas energy utilized by the LLTE, the heat absorbed by the air heater, and the CO_2 emission reduction are 60.97 MW, 40.44 MW, and 4.21 t/h, respectively. Between 16:00 and 07:00, the system remains relatively stable, with the LLTE utilizing approximately 85 MW of flue gas energy, the air heater absorbing around 54 MW of heat, and the CO_2 emission reduction fluctuating at about 5.3t/h. The load parameter variation of mode B is relatively large, as shown in subfigure (b). At the same time, the heat absorbed by the flue gas and the heat used by the heater show the same trend as the fgt. At 12:40, all values have been reduced to their lowest terms. The heat absorbed by the LLTE is 56.09 MW, while the heat absorbed by the air heater is 35.77 MW.

Fig. 9 illustrates the real-time variations of output power and thermal efficiency. The thermal efficiency increment and the additional work output per kilogram of coal follow the same trend. According to

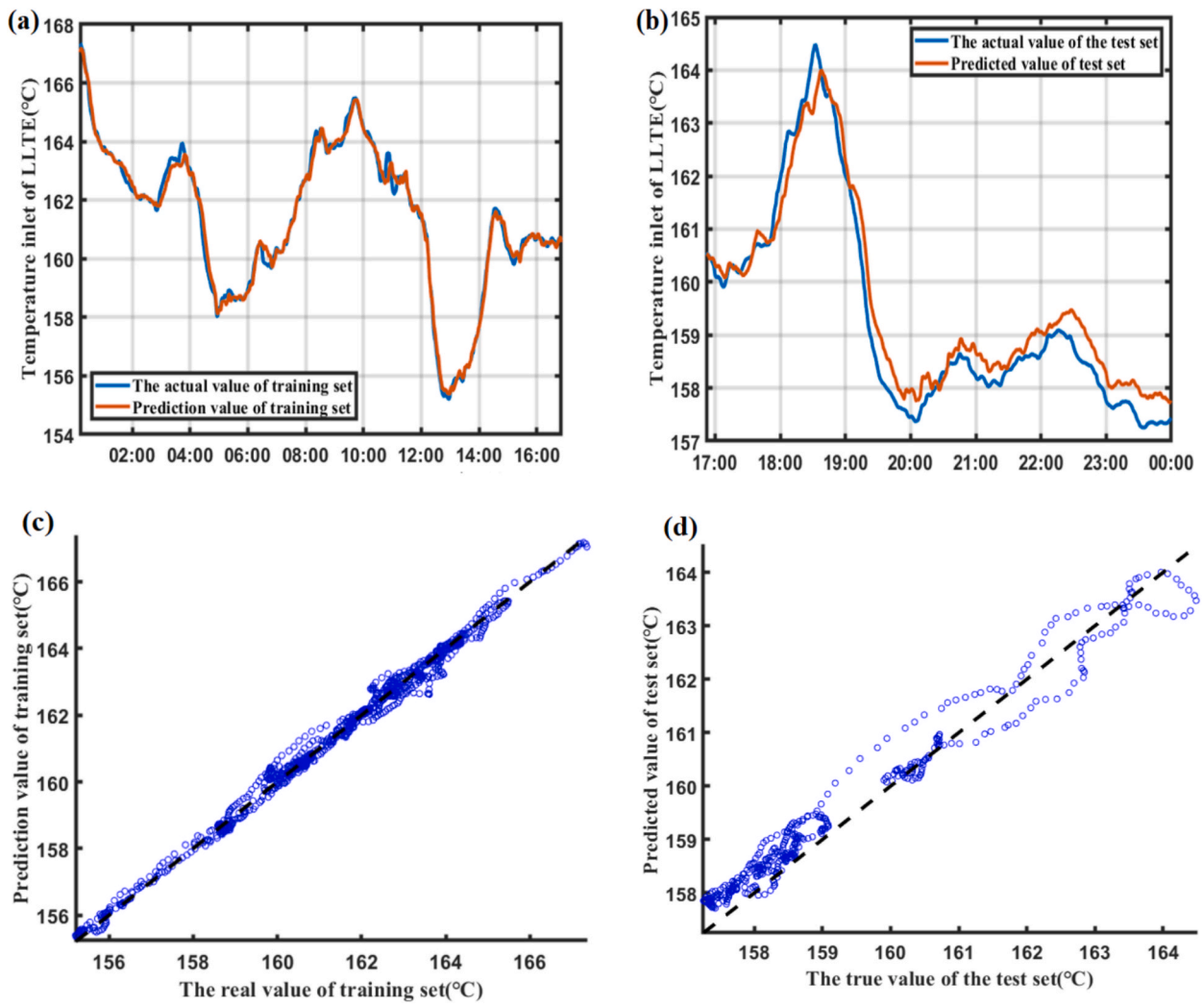

Fig. 12. Prediction of Fgt in Mode B.

Equations (2) and (3), changes in additional work output per kilogram of coal are determined by the flue gas enthalpy difference and the amount of recovered fgwh, both of which are influenced by output power. As output power increases, the utilization of fgwh rises, and the corresponding flue gas enthalpy difference increases accordingly. This leads to a greater increment in work output, thereby enhancing thermal efficiency. Under the two modes, the maximum values of the coal heat rate increment and the additional work output per kilogram of coal reached 110.10 kJ/kg and 0.926 %, 92.29 kJ/kg and 0.78 %, respectively.

Fig. 10 illustrates changes in coal consumption and heat consumption rate. Subfigures (a) and (b) show that the trends in coal consumption and heat consumption rate for power supply align with the trends in coal consumption saved. Mode A exhibits more stable overall changes compared to Mode B. Between 17:30 and 07:00, the output power, coal consumption for power supply, heat consumption rate, and reductions in coal consumption rate are 1003.23 MW, 265 g/kWh, 7066 kJ/kWh, and 2.65 g/kWh, respectively.

The flue gas heat utilized by the LLTE system is divided into two parts: one portion is used to heat the return water of the No. 6 LTE, while the other is used to preheat the cold secondary air. Higher energy levels correspond to better heat quality and more effective heat utilization. Regarding fgwh utilization, heating cold secondary air to return to the boiler for generating new steam represents the highest energy level, followed by the high-pressure water supply system, with the condensate system having the lowest thermal energy level. Therefore, when the heat released by the flue gas on the boiler side is certain, the best thermal efficiency should be to use the fgwh to heat the cold secondary air, increase the temperature of the hot air entering the boiler, reduce heat loss, and improve boiler efficiency.

When the fgt decreases, the energy utilized by the LLTE displaces more extraction steam, allowing additional steam to enter the turbine for power generation, thereby increasing the unit's thermal efficiency. At the same time, the rise in the outlet temperature of the air preheater further enhances boiler efficiency, leading to a greater system power output. According to Equation (13), the unit's coal consumption decreases as efficiency improves. This is consistent with the findings of Li et al(Li et al., 2023), who confirmed that after the integration of the LLTE, the increase in system power output is mainly attributed to the elevated steam enthalpy and the rise in preheated air temperature.

In Mode B, under optimized operation, the system output power is 920.09 MW, and coal consumption is reduced by 2.27 g/kWh. It is worth noting that starting from 10:30, the output power dropped sharply, resulting in a decrease in the unit's coal consumption for power supply and heat consumption rate. This decreased peaked at 12:40, when the coal consumption for power supply and heat consumption rate were 196.21 g/kWh and 5220 kJ/kWh, respectively.

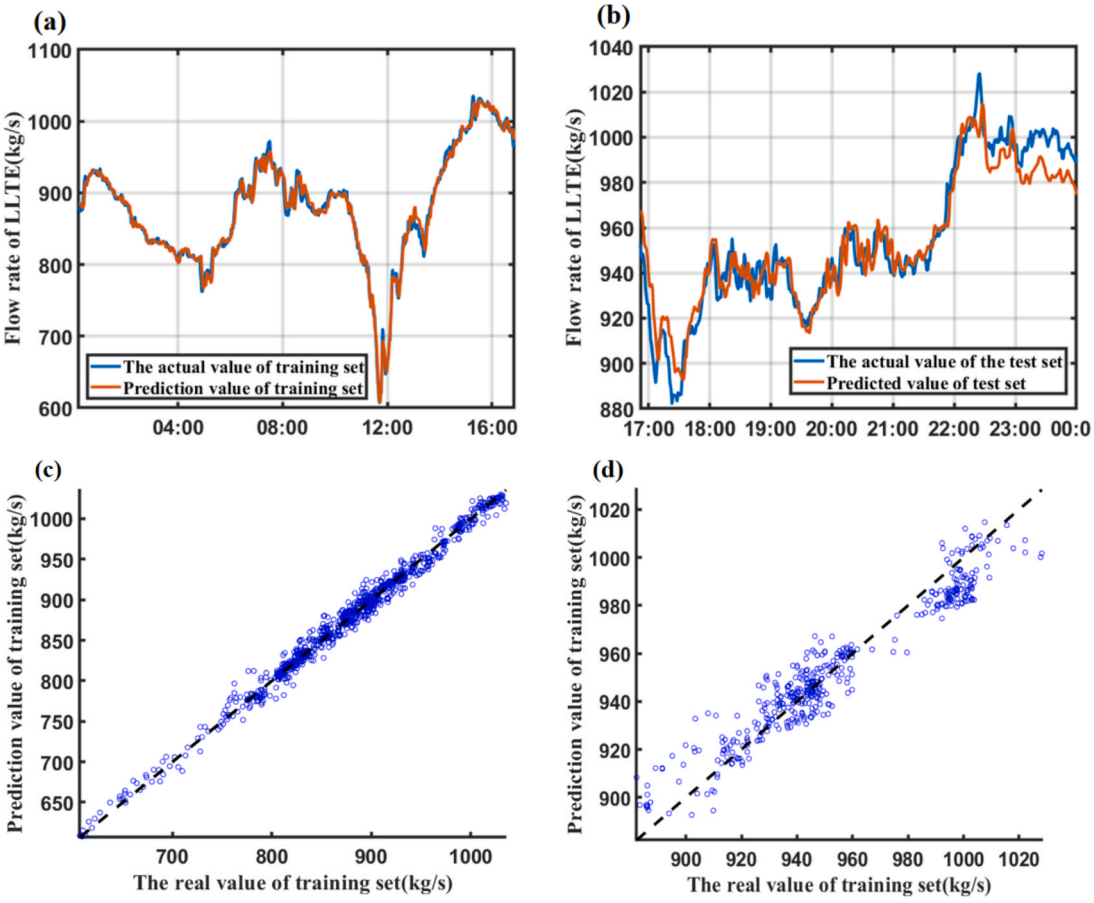

Fig. 13. Prediction of Flue Gas Flow Rate in Mode B.

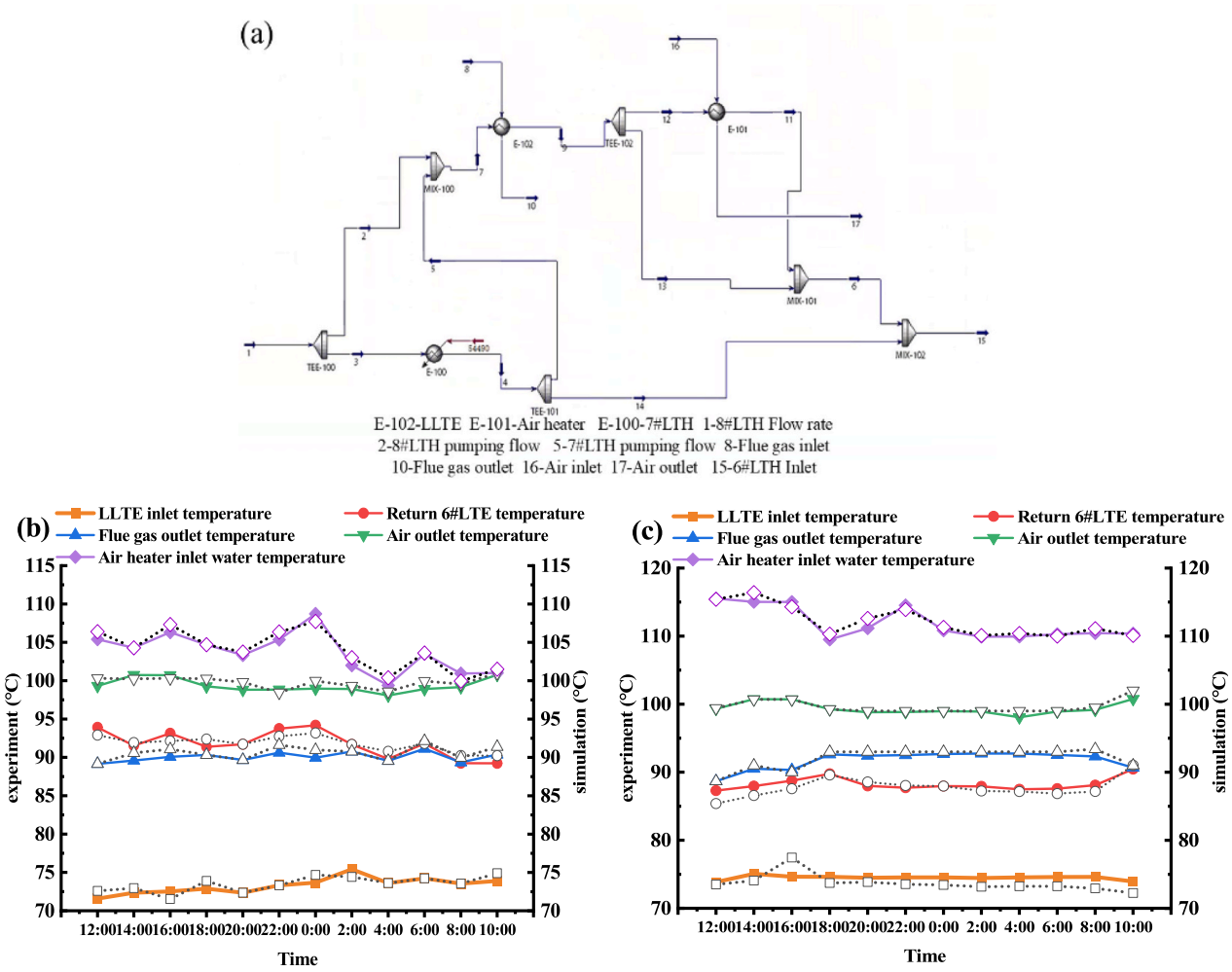

Fig. 14. Matlab linkage Hysys model verification.

5. Optimization analysis

5.1. Flue gas prediction

As a regression analysis method, LSSVM integrates the benefits of both the least squares method and SVM, offering more remarkable generalization ability compared to the traditional SVM (Sun, Lu, & Computation, 2024).

The CPO algorithm simulates crested porcupines' defense mechanisms and foraging behaviors to address complex optimization problems. Unlike Genetic Algorithms (GA) (Qasem & Lam, 2023) and Particle Swarm Optimization (PSO) (Jin et al., 2024), CPO uniquely integrates both local and global search capabilities, dynamically adjusting its search strategy to balance exploration and exploitation. This approach aims to identify global or near-global optimal solutions. Furthermore, circular population reduction technology speeds up convergence and helps maintain population diversity (Abdel-Basset, Mohamed, & Abouhawwash, 2024).

Due to the differences in units and the significant disparity in numerical values across the collected data, the model's accuracy is affected. Data preprocessing is an essential step before modeling. For instance, Yang et al. (Yang et al., 2025a; Yang et al., 2025b) adopted a de-centralization technique to enhance data consistency. In the present study, normalization is performed prior to modeling to eliminate dimensional discrepancies and ensure comparability across different data features, ensuring that all variables fall within the range of [0, 1]. The normalization method used is the min–max scaling method. For a given feature sequence x, the calculation formula is as follows:

$$x_{nor} = \frac{x - x_{\min}}{x_{\max} - x_{\min}} \tag{28}$$

x_{max} is the maximum value of the variable, $x_{\min}$ is the minimum value of the variable, and x_{nor} is the normalized data. During the evaluation of the four algorithms, several performance metrics are used for both the training and testing sets, including Root Mean Square Error (RMSE), Mean Absolute Error (MAE), and Mean Absolute Percentage Error (MAPE).

Various complex factors, including unit load, fuel and water supply conditions, air distribution methods, and the operating parameters of various heating surfaces, influence the LLTE inlet flue gas parameters. Based on the field conditions and boiler process requirements, the collected variables include 38 features such as the LLTE inlet flue gas parameters, generator power, secondary air outlet temperature, instantaneous total coal amount, total air volume, primary air volume, secondary air volume, furnace pressure, SOFA valve positions, and parameters of various heating surfaces. The specific details are listed in the table below (Table 7).

More significant fluctuations in flue gas parameters provide a better test of prediction accuracy. So, data from 00:00 to 17:00 is used as input for the two models, and the RMSE, MAE, and MAPE are selected as indicators to evaluate the prediction results. The prediction results for Mode A are described in Fig. 11. The RMSE, MAE, and MAPE of the CPO-LSSVM model for predicting the fgit of the LLTE under Mode A are 0.22, 0.19, and 0.11 %, respectively.

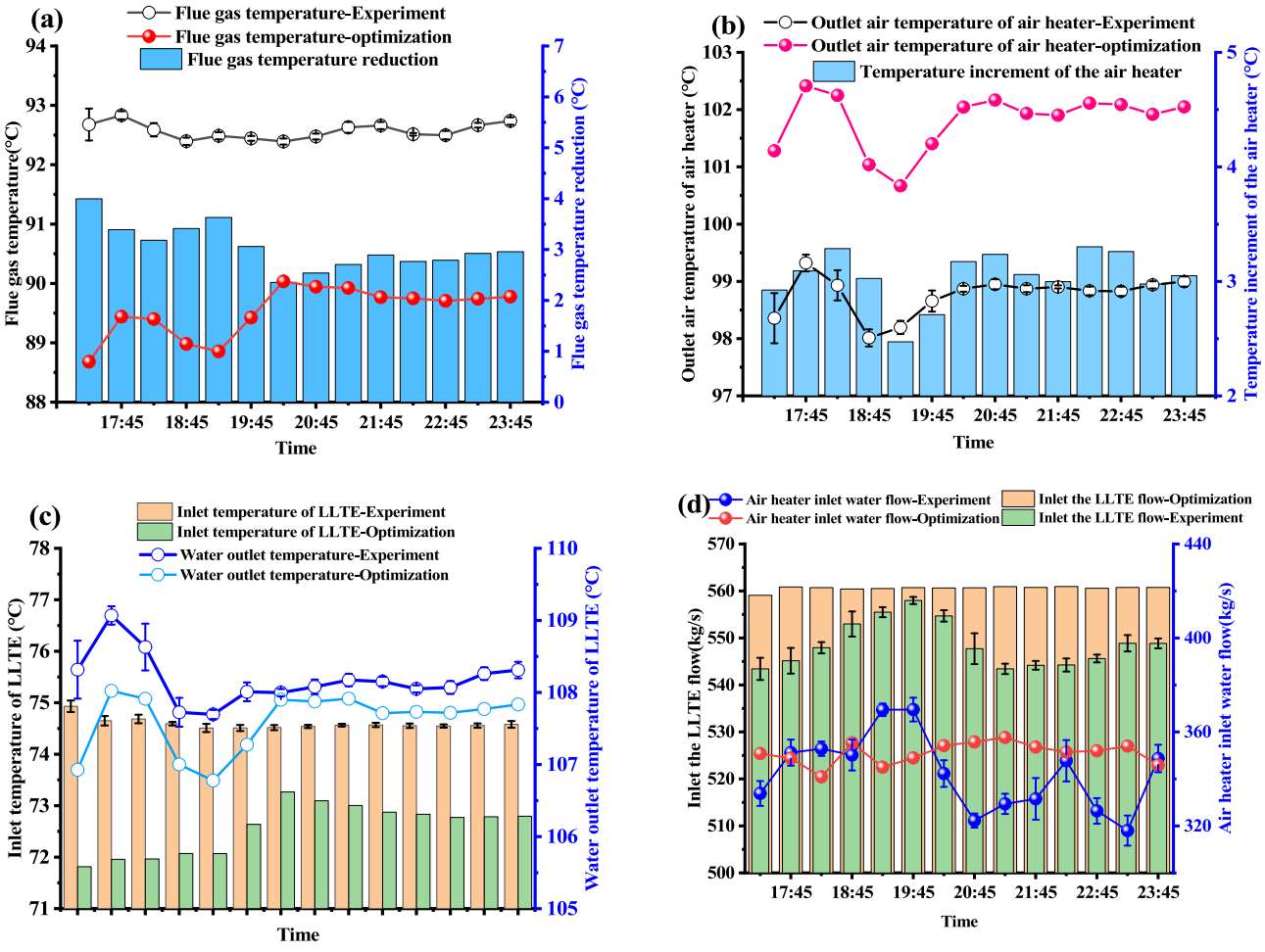

Fig. 15. A real-time analysis of the entrance and exit parameters for Mode A.

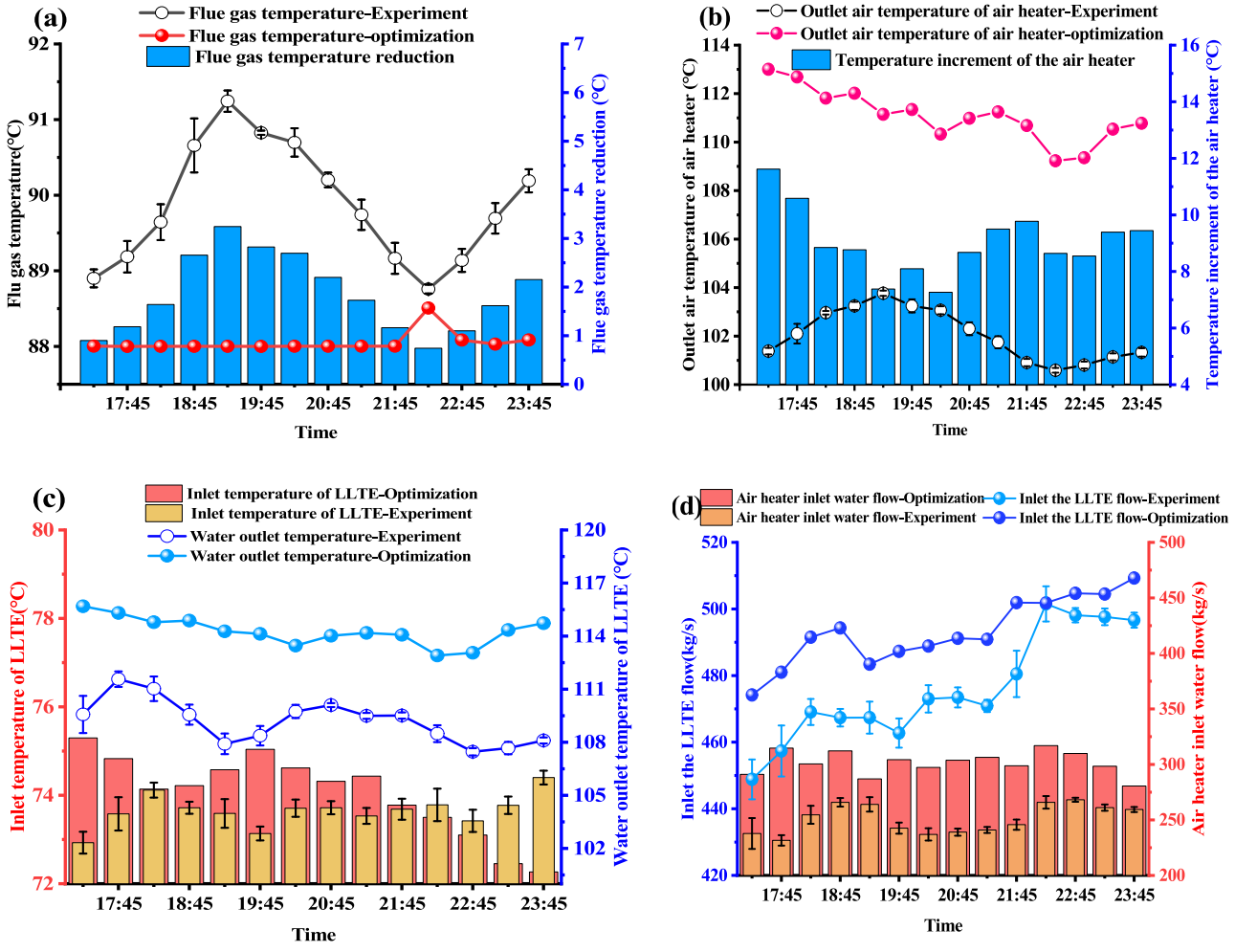

Fig. 16. A real-time analysis of the entrance and exit parameters for Mode B.

The experimental results show that the flue gas flow rate under Mode A is relatively stable, especially between 17:00 and 24:00. Consequently, data from this period is used directly for optimization.

Figs. 12 and 13 display the prediction results for flue gas parameters under Mode B. The CPO-LSSVM model's prediction errors for the fgit of LLTE are: RMSE of 0.43, MAE of 0.36, and MAPE of 0.23 %. For the flue gas inlet flow, the RMSE is 9.83, the MAE is 7.78, and the MAPE is 0.82 %. These indicators highlight the CPO-LSSVM model's high accuracy and precision in predicting the fgt and flow rate, demonstrating an excellent fit to actual data and providing a reliable basis for subsequent system operation and optimization.

5.2. Optimization analysis

Aspen HYSYS, with its advanced modeling capabilities and extensive physical property databases, supports dynamic simulations effectively. However, due to the volatility and significant lag in the regulation of flue gas, accurately predicting valve openings is challenging, which can lead to suboptimal utilization of fgwh. To address this issue, the CPO-LSSVM prediction model is utilized alongside the CPO algorithm and optimize HYSYS simulations. By adjusting the valve openings in advance, the real-time utilization of fgwh is significantly enhanced.

Fig. 14 compares experimental data with simulated data for the LLTE, the air heater, and the No. 6 LTE. Subfigure (a) shows the LLTE model, while subfigures (b) and (c) display simulation comparisons with experimental results under two different modes. The values of flue gas, heater, and 8#LTE inlet water temperature in the experimental data are employed as input variables. The model then predicted the inlet temperature of the LLTE, the fgot, and the inlet water temperature of the air heater, along with the return temperature for the 6# LTE. The results show that the model demonstrates excellent adaptability, with an overall error of less than 1 %.

Fig. 15 illustrates the real-time changes in the parameters for the LLTE and the air heater. Subfigure (a) shows that between 17:00 and 24:00, the average fgot in the experimental setup is 92.57 °C, whereas the optimized average temperature is 89.53 °C, reflecting a reduction of 3.04 °C. Additionally, as depicted in subfigure (c), the experimental temperature of the refrigerant water at the LLTE inlet is 74.59 °C, while the optimized inlet temperature of the refrigerant water is 72.56 °C. Furthermore, the experimental temperature of the LLTE heat medium outlet is 108.1 °C, compared to an optimized average temperature of 107.59 °C, indicating that the temperatures are virtually identical.

The author thinks this improvement is attributed to the benefits of a lower fgot. A reduced fgot enhances the waste heat recovery of the entire system, allowing for increased heating of refrigerant water and enabling more extracted steam to be utilized in the low-pressure cylinder for work. According to subfigure (b), the experimental heater outlet temperature is 98.76°C, while the optimized temperature is 101.81 °C, reflecting an increase of 3.04°C after optimization. As seen from subfigure (d), the experimental flow rate entering the heater and LLTE fluctuates widely, leading to significant exergy losses. The experimental flow rates for the LLTE and heater are 548.6 kg/s and 360 kg/s. After optimization, the flow rates into the LLTE and air heater become more stable at 560.6 kg/s and 342.5 kg/s, respectively.

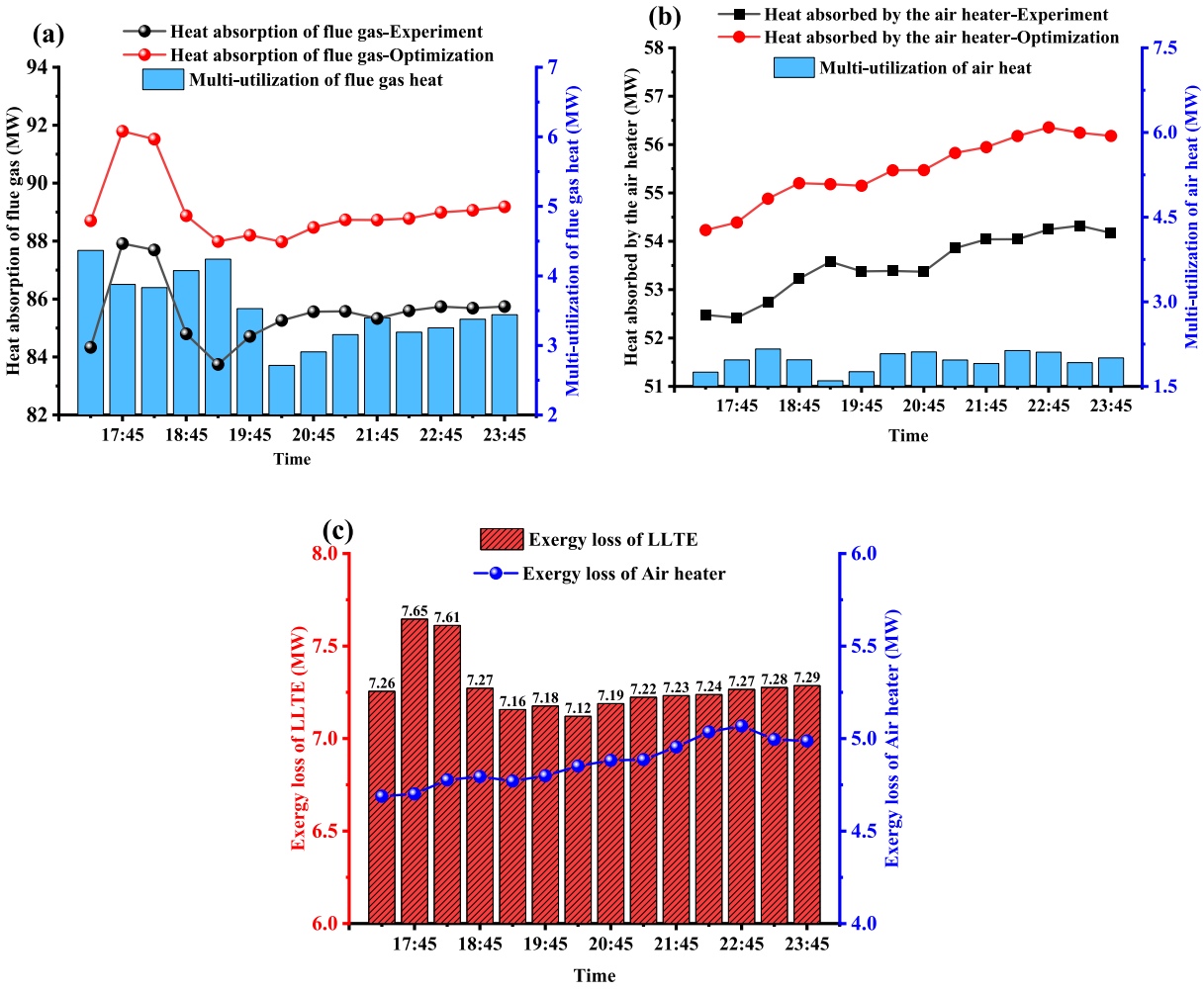

Fig. 17. Energy utilization analysis of LLTE and Air Heater under Mode A.

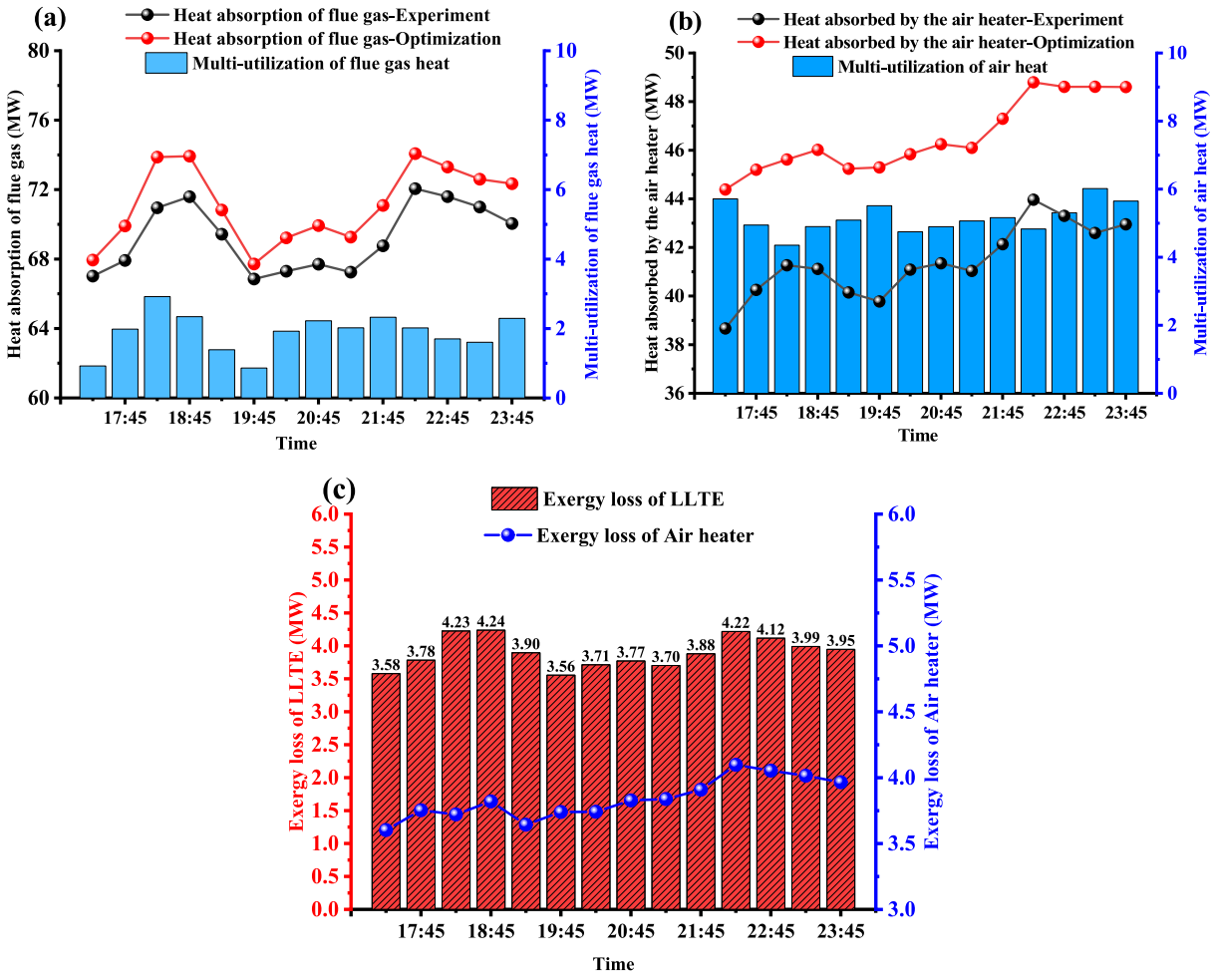

Fig. 18. Energy utilization analysis of LLTE and Air Heater under Mode B.

Fig. 16 illustrates the real-time changes in LLTE parameters following the optimization of mode B. Compared to the fluctuations observed in the experimental fgot, the optimized fgot is relatively stable, remaining around 88 °C. During this period, the average fgt decreased by 1.81 °C. which enhanced the utilization of fgwh, further reduced pollution, and conserved water. The experimental outlet temperature of the air heater stabilized at 102 °C. while the optimized outlet temperature increased to 111.1 °C. resulting in an average temperature rise of 9.1 °C.

Subfigure (d) explains this change more clearly. The average experimental flow rate of the heat medium entering the air preheater is 250 kg/s, while the optimized average flow rate increased to 301.57 kg/s. For the LLTE, the average experimental flow rate is 476.05 kg/s, and the optimized average flow rate rises to 493.21 kg/s. Under the same temperature rise conditions, the increased flow rate entering the LLTE further enhances the utilization of fgwh.

Figs. 17 and 18 illustrate the real-time energy change relationships between the LLTE and the air heater under two different operational modes. For mode A, the average utilization of experimental flue gas is 85.55 MW, with optimized utilization reaching 89.07 MW. After optimization, the average utilization of fgwh increased by 3.53 MW. The heat absorbed by the air heater during the experiment is 53.52 MW, which rises to 55.48 MW after optimization, reflecting an increase of 1.96 MW. The exergy loss in the LLTE and the air heater follows a similar trend to that of the absorbed heat. The enhanced heat exchange following optimization leads to higher flow rates of the heating water and enormous temperature difference between the inlet and outlet, resulting in increased exergy loss. After optimization, the average exergy losses are 7.28 MW for the LLTE and 4.87 MW for the air heater.

For Mode B, the average utilization of experimental flue gas is 69.25 MW, with the optimized utilization reaching 71.15 MW. This optimization results in an average increase of 1.90 MW in fgwh utilization. The heat absorbed by the air heater during the experiment is 41.40 MW, which increases to 46.56 MW after optimization, reflecting an increase of 5.16 MW. The exergy losses for the LLTE and the air heater are 3.90 MW and 3.84 MW, respectively.

Fig. 19 illustrates the relationship between thermal efficiency increments and work output under two modes: (a) and (b) correspond to Mode A, while (c) and (d) correspond to Mode B. According to Equations (3) and (4), the changes in thermal efficiency increment and output power are mainly determined by the enthalpy difference of the flue gas and the amount of recovered waste heat. As the output power increases, the available waste heat from the flue gas and the turbine efficiency improve, resulting in a greater flue gas enthalpy difference. Consequently, more work is produced per kilogram of coal, and the thermal efficiency increment also rises.

For Mode A, the overall load remained stable during the observed period. After optimization, the average additional work output per kilogram of coal is 119.68 kJ/kg, representing an increase of 12 kJ/kg compared to the baseline. The average thermal efficiency increment is 1.023 %, with a gain of 0.103 % over the baseline. In Mode B, between 17:00 and 24:00, the output power increased, leading to corresponding rises in both the thermal efficiency increment and the additional work output per kilogram of coal. After optimization, the experimental average of additional work output per kilogram of coal is 88.44 kJ/kg, with an increase of 11.2 kJ/kg compared to the baseline. The average

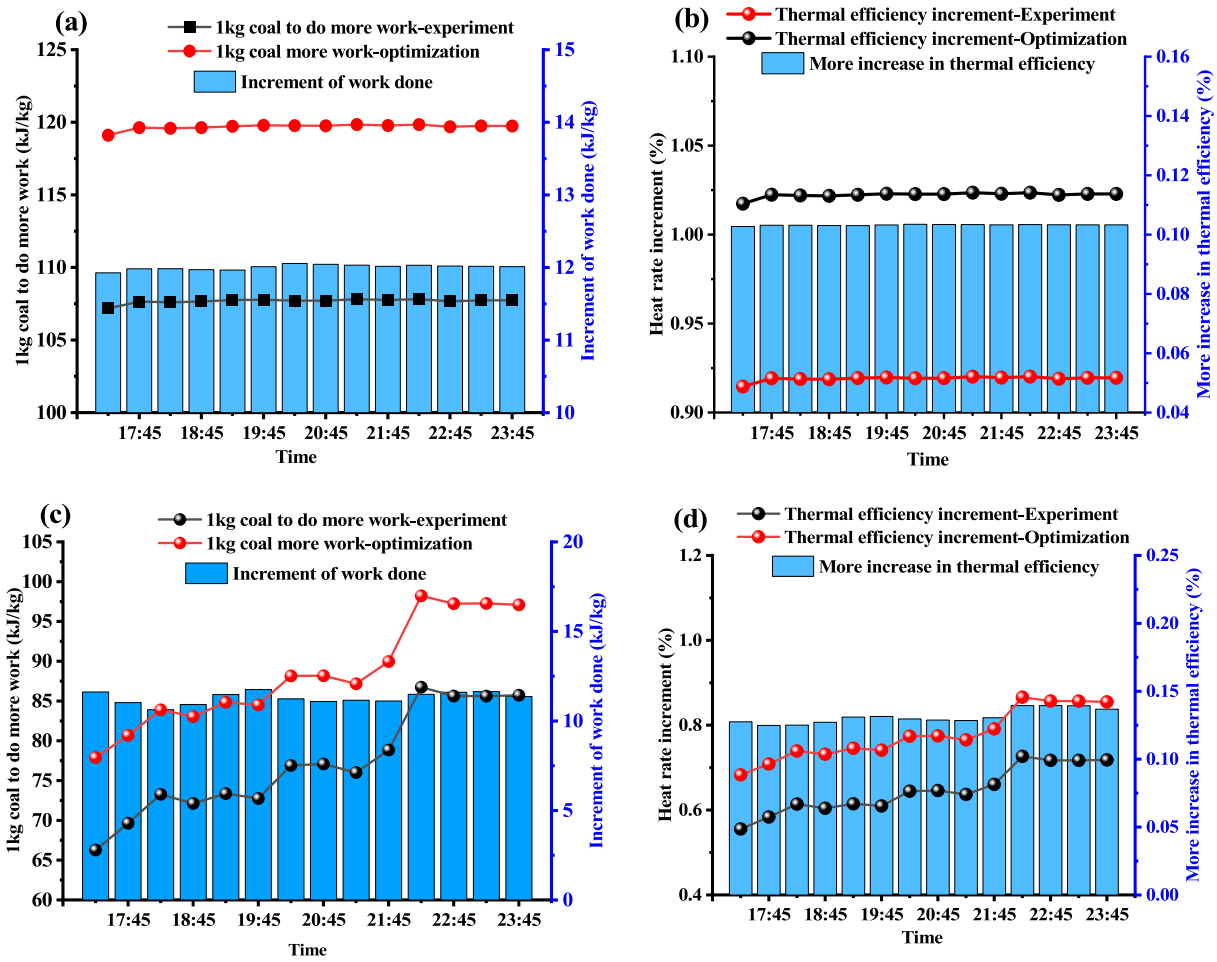

Fig. 19. Thermal Efficiency Increment and Work Analysis.

thermal efficiency increment is 0.778 %, reflecting an improvement of 0.131 % over the baseline.

The relationship between power supply, coal consumption, heat consumption rate, and emission reduction are shown in Fig. 20. Coal savings mainly depend on the boiler thermal efficiency increment and output power; the higher the output power, the larger the corresponding coefficient b1. For Mode A, between 17:00 and 24:00, the output power remained relatively stable at around 1000 MW. Combined with the thermal efficiency changes shown in Fig. 19, the coal savings reached 2.81 g/kWh after optimization, an improvement of 0.28 g/kWh compared to the baseline. The power supply coal consumption followed the same trend.

The traditional PID control did not enable the LLTE to achieve optimal utilization of fgwh. After optimization using CPO-LSSVM, the flow rate of cold media water entering the LLTE increased, further enhancing the utilization of fgwh, reducing steam extraction, and saving coal consumption. According to Equation (12), the thermal efficiency increment mainly depends on the power supply coal consumption. After optimization, the heat rate during this period is 7055.63 kJ/kWh, a 7.55 kJ/kWh reduction compared to the baseline. The CO_2 reduction is 10.28 t/h, an improvement of 1.04 t/h over the baseline.

Fig. 21 presents the economic analysis under Mode B. As output power increases, coal savings gradually rise, reaching a maximum of 2.51 g/kWh at 22:15. At this point, the corresponding values for power supply coal consumption, heat rate, and CO_2 reduction also peak at 237.15 g/kWh, 6309.05 kJ/kWh, and 8.23 t/h, respectively. After optimization, the coal savings, power supply coal consumption, heat rate, and CO_2 reduction each showed improvements of 0.38 g/kWh, 0.38 g/kWh, 10.15 kJ/kWh, and 1.19 t/h, respectively, compared to the baseline averages.

6. Conclusion

This paper presents an experimental study on the capacity expansion and transformation of a 1000 MW thermal power unit, focusing on the influence of integrating an LLTE with a secondary air heater system on crucial parameters such as thermal efficiency, output power, and coal consumption. Additionally, to address the regulation lag following capacity expansion, a CPO-LSSVM intelligent vector regression model is employed to predict the flue gas parameters of the LLTE in real-time. Based on these predictions, optimization analysis is performed using Matlab and Hysys software. The key findings are summarized as follows:

(1) In the experimental study of capacity expansion, under the optimized operation of Mode A, the system output power reaches 1003.23 MW, with a thermal efficiency increment of 0.93 %. Coal consumption reduction is increased by 2.69 g/kWh, and CO_2 emissions reduction is increased by 9.88 t/h. In Mode B, under optimized operation, the system output power is 920.09 MW, the thermal efficiency improves by 0.87 %, and coal consumption is reduced by 2.27 g/kWh, and the CO_2 emissions reduction is increased by 7.64 t/h.

(2) In predicting flue gas parameters, RMSE, MAE, and MAPE are used as evaluation metrics. The results indicate that the CPO-LSSVM model excels in forecasting the flue gas parameters. Specifically, the RMSE for the CPO-LSSVM model in predicting the fgit under Mode A is 0.22, while under Mode B is 0.43.

(3) After optimization employing Hysys combined with Matlab, the

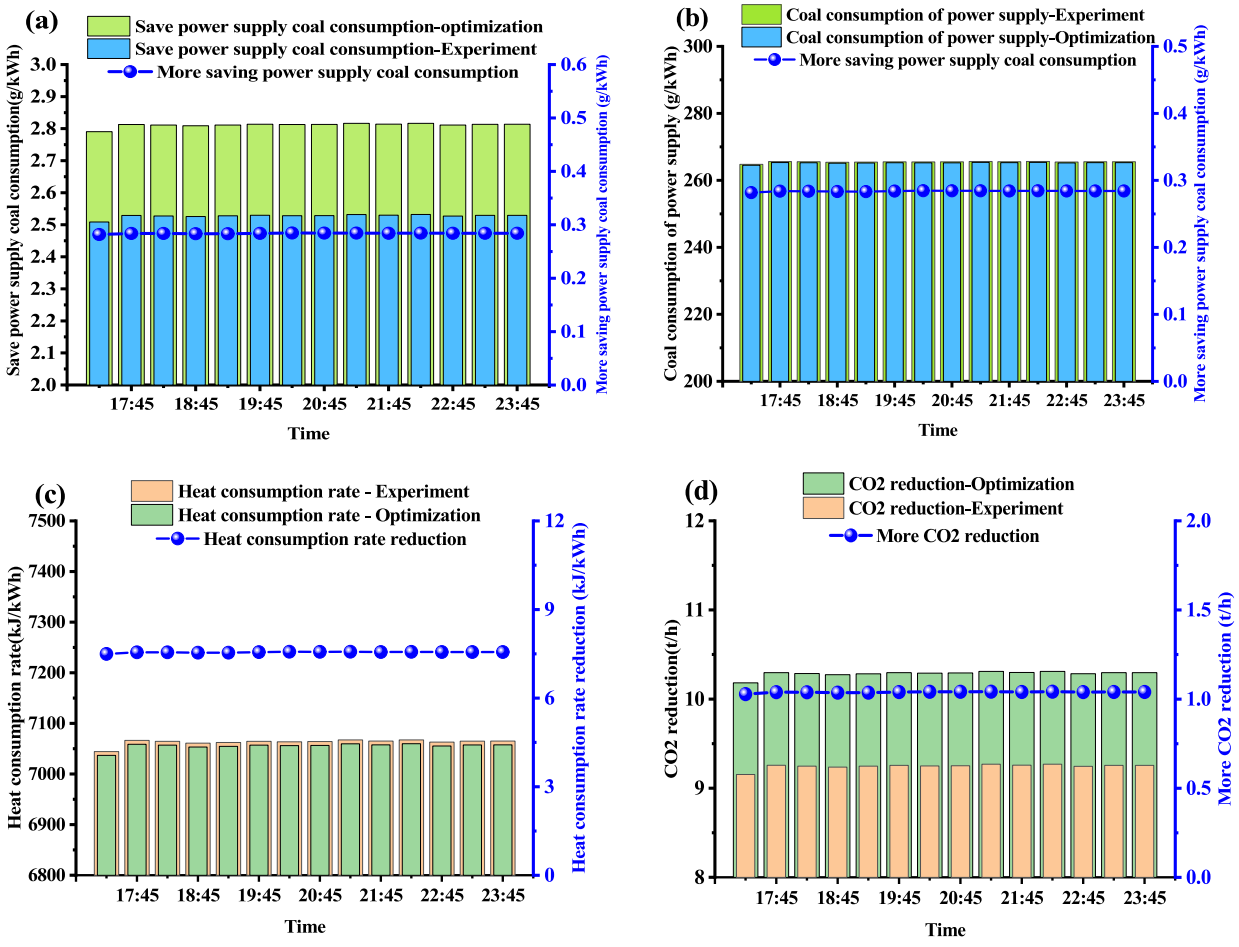

Fig. 20. Model A economic analysis.

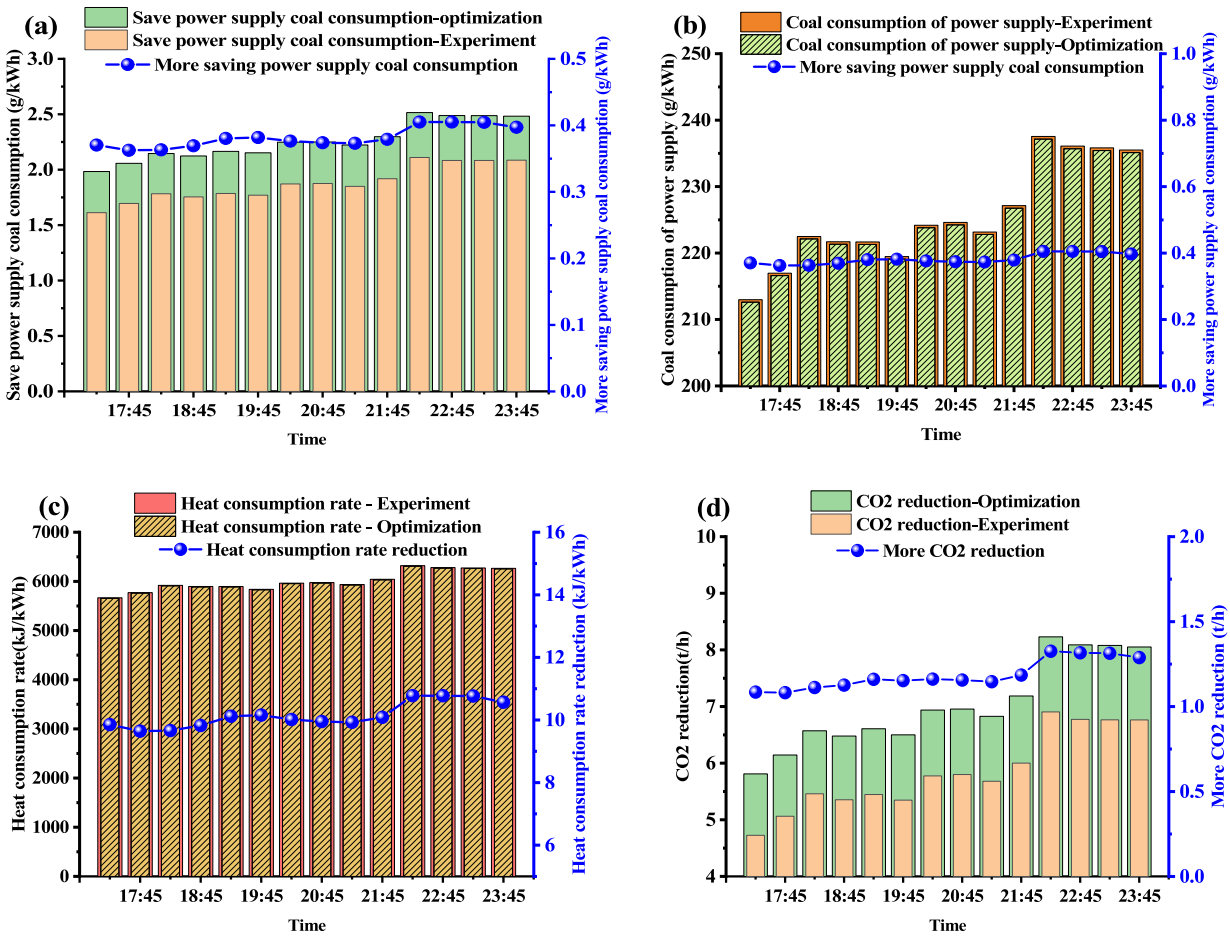

Fig. 21. Model B economic analysis.

results under Mode A show that the fgot is 89.53 °C. which is 3.04 °C lower than the experimental value. The outlet temperature of the air heater is 101.8 °C. increasing 3.04 °C than the experimental value. The fgwh is 89.07 MW, exceeding the experimental value by 3.53 MW. Saving coal consumption reduction is 2.81 g/kWh, higher by 0.28 g/kWh than the experimental value. CO2 reduction is 10.28 t/h, an increase of 1.04 t/h compared to the experiment, and thermal efficiency improved by 0.103 %.

(4) Under the optimized operation of Mode B, the fgot is 89.86 °C. 1.81 °C lower than the experimental value, while the air heater outlet temperature is 111.08 °C. which is 9.04 °C higher than the experimental value. The fgwh utilized from the flue gas is 71.15 MW, exceeding the experimental value by 1.90 MW. The coal consumption for power supply reduction is 2.51 g/kWh, 0.4 g/kWh higher than the experimental value. CO_2 reduction reaches 8.23 t/h, which is 1.32 t/h higher than the experimental value, and thermal efficiency improves 0.87 %, which is 0.14 % higher than the experimental value.

The CPO algorithm requires empirical tuning of hyperparameters such as population size and mutation rate. Improper settings can lead to premature convergence or excessively slow optimization. Many power plants have already undergone cogeneration (steam-electric dual-drive) retrofitting. In such systems, low-temperature fgwh recovered by the LLTE and Air Heater is partly used to preheat the cold secondary air before it returns to the boiler, while the rest is used to heat the feedwater for the No. 7 LTH and No. 8 LTH, which then returns to the "water side" of the No. 6 LTH. Meanwhile, the exhaust steam from the cogeneration system returns to the "gas side" of the No. 6 LTH. This creates a conflict between the "water side" and "gas side" of the No. 6 LTH. Determining the optimal steam-water distribution ratio under varying unit loads will be the focus of the next phase of work.

CRediT authorship contribution statement

Huaan Li: Conceptualization, Formal analysis, Methodology, Writing – original draft. **Dongliang Wei:** Data curation, Formal analysis, Methodology, Validation. **Yajie Wu:** Methodology, Validation, Visualization. **Hui Li:** Data curation, Software. **Hongtao Liu:** Investigation, Validation. **Xiaolin Hu:** Investigation, Visualization. **Huanxiang Zhang:** Investigation, Software. **Hao Zhou:** Project administration, Supervision.

Declaration of competing interest

The authors declare that they have no known competing financial interests or personal relationships that could have appeared to influence the work reported in this paper.

Acknowledgments

This work was supported by the Fundamental Research Funds for the Central Universities (2022ZFJH04).

Data availability

Data will be made available on request.

References

Abdel-Basset, M., Mohamed, R., & Abouhawwash, M.-J.-K.-B.-S. (2024). Crested porcupine optimizer: A new nature-inspired metaheuristic. *Knowledge-Based Systems, 284*, Article 111257.

Al-Dahidi, S., Alrbai, M., Al-Ghussain, L., & Alahmer, A. J. A. E. (2024). Maximizing energy efficiency in wastewater treatment plants: A data-driven approach for waste heat recovery and an economic analysis using Organic Rankine Cycle and thermal energy storage. *Applied Energy, 362*, Article 123008.

Chantasiriwan, S. (2021). Optimum installation of economizer, air heater, and flue gas dryer in biomass boiler. *Computers & Chemical Engineering, 150*, Article 107328. https://doi.org/10.1016/j.compchemeng.2021.107328

Chen, X., Wang, X., Ding, T., & Li, Z. J. A. E. (2023). Experimental research and energy saving analysis of an integrated data center cooling and waste heat recovery system. *Applied Energy, 352*, Article 121875.

Dong, S., Hu, X., Huang, J. F., Zhu, T., Zhang, Y., & Li, X. J. E. (2021). Investigation on improvement potential of ORC system off-design performance by expander speed regulation based on theoretical and experimental exergy-energy analyses. *Energy, 220*, Article 119753.

Espatolero, S., Cortés, C., & Romeo, L. M. J. A. E. (2010). Optimization of boiler cold-end and integration with the steam cycle in supercritical units. *Applied Energy, 87*(5), 1651–1660.

Fan, C., Pei, D., & Wei, H. (2018). A novel cascade energy utilization to improve efficiency of double reheat cycle. *Energy Conversion and Management, 171*, 1388–1396.

Han, X., Yuan, T., Zhang, D., Dai, Y., Liu, J., & Yan, J. (2021). Waste heat utilization from boiler exhaust gases for zero liquid discharge of desulphurization wastewater in coal-fired power plants: Thermodynamic and economic analysis. *Journal of Cleaner Production, 308*, Article 127328. https://doi.org/10.1016/j.jclepro.2021.127328

Han, X., Yuan, T., Zhang, D., Dai, Y., Liu, J., & Yan, J. J. J. (2021). Waste heat utilization from boiler exhaust gases for zero liquid discharge of desulphurization wastewater in coal-fired power plants. *Thermodynamic and Economic Analysis, 308*, Article 127328.

Han, Y., Xu, G., Zheng, Q., Xu, C., Hu, Y., Yang, Y., & Lei, J. J. A. T. E. (2017). New heat integration system with bypass flue based on the rational utilization of low-grade extraction steam in a coal-fired power plant. *Applied Thermal Engineering, 113*, 460–471.

Huang, L., Chen, G., Xu, X., Tan, R., Gao, X., Zhang, H., & Yu, J. (2024). Recovering low-grade heat from flue gas in a coal-fired thermal power unit. *Energies, 17*(20). https://doi.org/10.3390/en17205204

Jin, X., Wei, B., Deng, L., Yang, S., Zheng, J., & Wang, F. (2024). An adaptive pyramid PSO for high-dimensional feature selection. *Expert Systems with Applications, 257*, Article 125084.

Lee, S., Chung, Y., Kim, S., Jeong, Y., & Kim, M. (2023). Predictive optimization method for the waste heat recovery strategy in an electric vehicle heat pump system. *Applied Energy, 333*, Article 120572.

Li, Y., Chen, X., Jiang, S., & Lu, G. (2023). Thermodynamics of cascaded waste heat utilization from flue gas and circulating cooling water. *Journal of Thermal Science, 32*(6), 2166–2178.

Liu, G., Zhao, H., Wang, Z., Abdulwahid, A. A., & Han, J. (2022). Performance study and multi-objective optimization of a two-temperature CO_2 refrigeration system with economizer based on energetic, exergetic and economic analysis. *Journal of Thermal Science, 31*(5), 1416–1433. https://doi.org/10.1007/s11630-022-1696-4

Lu, T., Lü, X., Välisuo, P., Zhang, Q., & Clements-Croome, D. J. A. E. (2024). Innovative approaches for deep decarbonization of data centers and building space heating networks: Modeling and comparison of novel waste heat recovery systems for liquid cooling systems. *Applied Energy, 357*, Article 122473.

Ma, H., Liang, N., Liu, Y., Luo, X., Hou, C., & Wang, G. (2021). Experimental study on novel waste heat recovery system for sulfide-containing flue gas. *Energy, 227*, Article 120479.

Muriuki, L., Wekesa, D. W., & Njoka, F. J. (2024). Modeling, simulation and techno-economic evaluation of a micro-grid system based on steam gasification of organic municipal solid waste. *Energy Conversion and Management, 299*, Article 117813.

Ouyang, T., Xu, J., Su, Z., Zhao, Z., Huang, G., & Mo, C. (2021). A novel design of low-grade waste heat utilization for coal-fired power plants with sulfuric acid recovery. *Energy Conversion and Management, 227*, Article 113640.

Pan, Q., Peng, J., Wang, H., Sun, H., & Wang, R. J. S. E. (2019). Experimental investigation of an adsorption air-conditioner using silica gel-water working pair. *Solar Energy, 185*, 64–71.

Qasem, A. G., & Lam, S. S. (2023). Prediction of wart treatment response using a hybrid GA-ensemble learning approach. *Expert Systems with Applications, 221*, Article 119737.

Saoud, A., Bruno, J. C., Boukhchanaa, Y., & Fellah, A. J. A. T. E. (2023). Performance investigation and numerical evaluation of a single-effect double-lift absorption chiller. *Applied Thermal Engineering, 227*, Article 120369.

Stevanovic, V. D., Petrovic, M. M., Wala, T., Milivojevic, S., Ilic, M., & Muszynski, S. J. E. (2019). Efficiency and power upgrade at the aged lignite-fired power plant by flue gas waste heat utilization: High pressure versus low pressure economizer installation. *Energy, 187*, Article 115980.

Stevanovic, V. D., Wala, T., Muszynski, S., Milic, M., & Jovanovic, M. (2014). Efficiency and power upgrade by an additional high pressure economizer installation at an aged 620 MWe lignite-fired power plant. *Energy, 66*, 907–918.

Sun, H., & Lu, Y. (2024). A novel approach for solving linear Fredholm integro-differential equations via LS-SVM algorithm. *Applied Mathematics and Computation, 470*, Article 128557.

Tan, H., Cao, R., Wang, S., Wang, Y., Deng, S., & Duić, N. (2021). Proposal and techno-economic analysis of a novel system for waste heat recovery and water saving in coal-fired power plants: A case study. *Journal of Cleaner Production, 281*, Article 124372. https://doi.org/10.1016/j.jclepro.2020.124372

Tang, H., Liu, M., Zhang, K., Zhang, S., Wang, C., & Yan, J. (2024). Performance evaluation and operation optimization of a combined heat and power plant integrated with molten salt heat storage system. *Applied Thermal Engineering, 245*, Article 122848. https://doi.org/10.1016/j.applthermaleng.2024.122848

Wang, Z., Pan, H., Xia, X., Xie, B., Peng, D., & Yang, H. J. E. (2022). Experimental investigation on steady and dynamic performance of organic Rankine cycle with R245fa/R141b under different cooling and expander speed conditions. *Energy, 241*, Article 122511.

Weitzer, M., Müller, D., Steger, D., Charalampidis, A., Karellas, S., & Karl, J. J. E. C. (2022). Organic flash cycles in Rankine-based Carnot batteries with large storage temperature spreads. *Energy Conversion and Management, 255*, Article 115323.

Xiao, P., Zhang, Y., Wang, Y., & Wang, J. (2019). Analysis of an improved economizer system for active control of the coal-fired boiler flue gas temperature. *Energy, 170*, 185–198.

Xu, G., Xu, C., Yang, Y., Fang, Y., Li, Y., & Song, X. (2014). A novel flue gas waste heat recovery system for coal-fired ultra-supercritical power plants. *Applied Thermal Engineering, 67*(1–2), 240–249.

Xu, W., Jin, Y., Zhu, L., & Li, Z. (2021). Performance analysis of the technology of high-temperature boiler feed water to recover the waste heat of mid-low-temperature flue gas. *ACS Omega, 6*(40), 26318–26328.

Yan, M., Zhang, L., Shi, Y., Zhang, L., Li, Y., & Ma, C. J. E. (2018). A novel boiler cold-end optimisation system based on bypass flue in coal-fired power plants: Heat recovery from wet flue gas. *Energy, 152*, 84–94.

Yang, B., Lei, Y., Li, N., Li, X., Si, X., & Chen, C. (2025a). Balance recovery and collaborative adaptation approach for federated fault diagnosis of inconsistent machine groups. *Knowledge-Based Systems, 317*, Article 113480. https://doi.org/10.1016/j.knosys.2025.113480

Yang, B., Lei, Y., Li, X., Li, N., Si, X., & Chen, C. (2025b). A dynamic barycenter bridging network for federated transfer fault diagnosis in machine groups. *Mechanical Systems and Signal Processing, 230*, Article 112605. https://doi.org/10.1016/j.ymssp.2025.112605

Yang, M.-H., & Yeh, R.-H.-J.-E. (2022). Investigation of the potential of R717 blends as working fluids in the organic Rankine cycle (ORC) for ocean thermal energy conversion (OTEC). *Energy, 245*, Article 123317.

Yang, Y., Xu, C., Xu, G., Han, Y., Fang, Y., & Zhang, D. (2015). A new conceptual cold-end design of boilers for coal-fired power plants with waste heat recovery. *Energy Conversion and Management, 89*, 137–146.

Zhang, G., Zhang, S., Sun, B., Liu, J., & Yan, J. (2024). Design on a novel waste heat recovery system integrated with the bypass flue and outside primary air preheater for bitumite-fired power plants. *Energy, 291*, Article 130341.

Zhang, H.-H., Zhang, Y.-F., Feng, Y.-Q., Chang, J.-C., Chang, C.-W., Xi, H., & Li, M.-J.-J.-E. (2023). The parametric analysis on the system behaviors with scroll expanders employed in the ORC system: An experimental comparison. *Energy, 268*, Article 126713.